JOURNAL OF GEOPHYSICAL RESEARCH, VOL. 97, NO. C7, PAGES 11,299–11,321, JULY 15, 1992

# Laboratory Simulation of Exchange Through Fram Strait

KENNETH HUNKINS

*Lamont-Doherty Geological Observatory of Columbia University, Palisades, New York*

J. A. WHITEHEAD

*Woods Hole Oceanographic Institution, Woods Hole, Massachusetts*

Laboratory experiments and theory were conducted to observe the flow patterns and transport in both buoyancy-driven and wind-driven rotating fluids. In "lock-exchange" experiments, water with one density flows into a second basin after a sliding gate is removed. Water of a second density flows back into the first basin. The size and location of the currents for various values of density difference, rotation rate, and assorted sidewall geometries was recorded. Volume flux of the fluid was also measured and compared with a theory for lock-exchange flow of a rotating fluid. In a separate group of experiments with a passive upper layer, easterly winds (like those in the Arctic Ocean) drive the upper level water into the Arctic Ocean and therefore oppose the buoyant exchange. Westerly winds would drive the water out of the Arctic Ocean. This indicates that the exchange between the Arctic Ocean and the Greenland-Norwegian Sea is likely to be driven by buoyancy rather than by driven by wind. Crude estimates of the volumetric and fresh water exchange rate from the lock-exchange formulas are compared with observed ocean fluxes, and approximate agreement is found.

## INTRODUCTION

The seas in high northern latitudes have a special interest for oceanography because they provide a major heat sink for the world ocean and are an important component of global convection and climate. In recognition of this important role there has been increasing attention in recent years to both observational and modeling programs for the Arctic Ocean and the Greenland Sea. The severe climate and the presence of sea ice, particularly in the Arctic Ocean, severely restrict field operations, so oceanographic data have accumulated slowly and are still quite limited. It is necessary to extract as much information as possible from the data available and to interpret them with theoretical models designed to test ideas about the physical processes. Simple laboratory models of the Arctic Ocean and Greenland Sea will be described here which have been developed with the object of clarifying ideas about their circulation and the exchange between them. These models explore idealized situations based on relevant physical concepts but are not designed to realistically mimic currents and hydrography. They are expected to contribute toward agreement on the nature of the important physical processes in these oceans, to stimulate more detailed modeling, and to aid in planning future field exploration.

Before describing the model experiments we will review briefly the oceanography of the seas on which these studies focus. The deep basins of the Arctic Ocean and the Greenland Sea are connected by the gap between Greenland and Spitsbergen known as Fram Strait. This opening is 450 km wide across its narrowest section with depths exceeding 2000 m for a distance of 100 km along that same section (Figure 1). Thus, despite its name, Fram Strait lacks the narrow width and shallow depth usually associated with the term strait and cannot be expected to exert the same kind of control on exchange that, for example, the Strait of Gibraltar exerts on flow between the Atlantic Ocean and the Mediterranean Sea. Ice and Arctic waters flow southward through Fram Strait while Atlantic waters flow northward. Much of this transfer takes place in two narrow boundary currents. The East Greenland Current on the western side of the strait exports cold water of low salinity from the Arctic Ocean to the Greenland Sea and the West Spitsbergen Current on the eastern side carries warm saline waters northward. Strong fronts in the strait separate the two principal contrasting water masses which have their origins, respectively, in high polar latitudes and in the subtropics. Within these seas there is a wide range of mesoscale motion superimposed on the mean flow. In Fram Strait, transient propagating eddies with diameters ranging from several kilometers to 100 km have frequently been observed along the marginal ice zone both in remotely sensed images and in hydrographic surveys [*Johannessen et al.*, 1987; *Manley, et al.*, 1987*a*; *Ginsberg and Fedorov*, 1989]. Meanders of both the ice edge and the front along the East Greenland Current are commonly seen, and one subice meander was seen to develop into a cyclonic eddy [*Manley et al.*, 1987*b*]. Another type of feature is the nearly stationary eddy which has often been observed over the Molloy Deep in the northern central part of the strait. This cyclonic eddy is about 60 km across and seems to be topographically trapped [*Wadhams and Squire*, 1983; *Bourke et al.*, 1987].

Despite its lack of a sill or narrow constriction, Fram Strait does appear to act as a barrier to exchange since strong contrasts exist between the water masses of the Arctic Ocean and Greenland Sea. The Arctic Ocean is covered in its deep regions with perennial drifting sea ice and an upper water layer about 100 m thick with salinity of only 31 to 32 ppt (Figure 2). This upper layer, freshened by river runoff from surrounding continents, forms a cold, low-salinity lens which overlies a transition layer of increasing salinity and density between 100 and 300 m. The lid of low-salinity water on the Arctic Ocean prevents convective circulation

Paper number 92JC00735.
0148-0227/92/92JC-00735$05.00

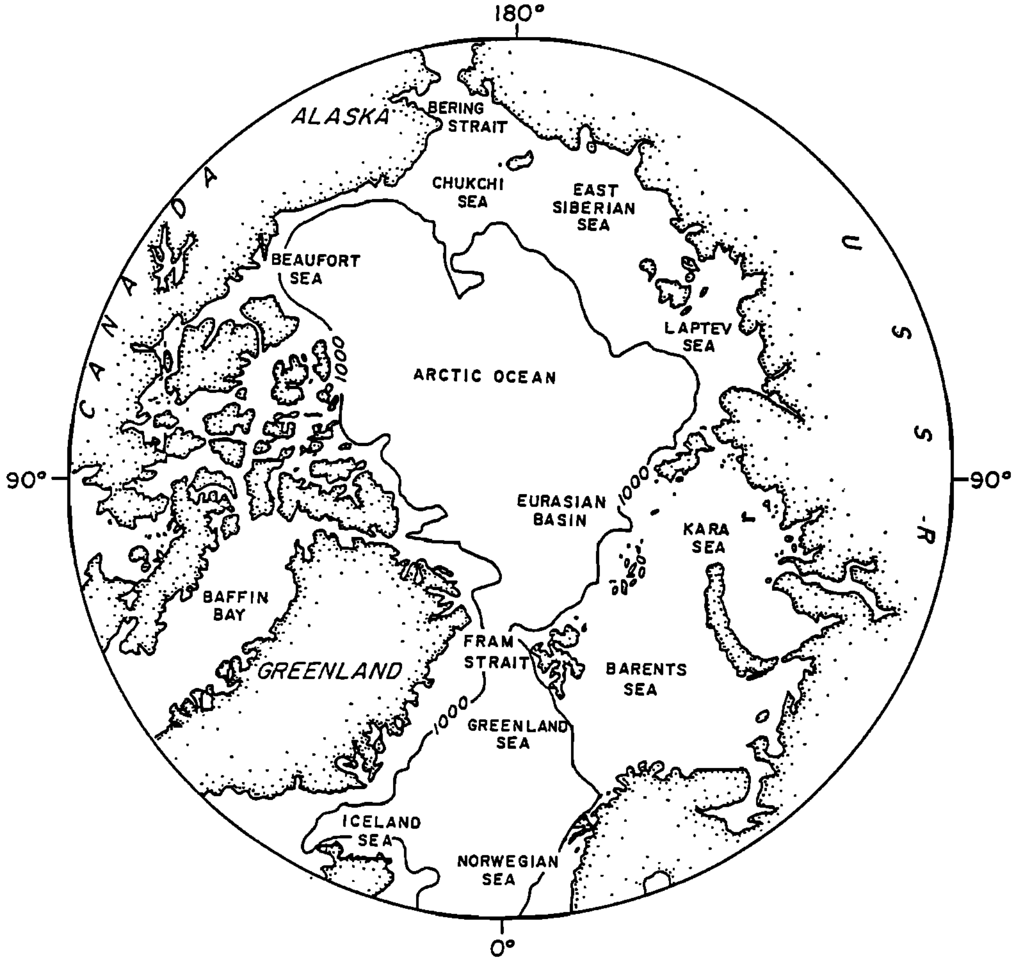

Fig. 1. Bathymetry of the Arctic Ocean and Greenland Sea.

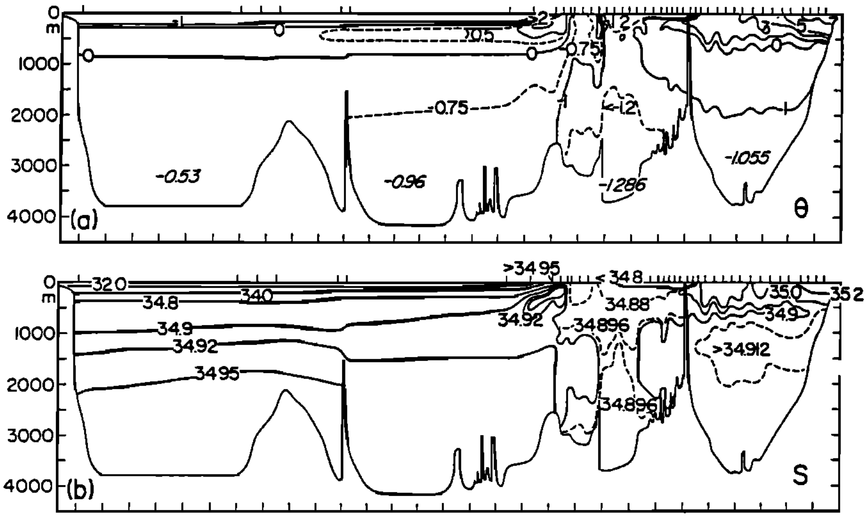

Fig. 2. Potential temperature and salinity sections across the Arctic Ocean and the Greenland and Norwegian Seas (adapted from *Aagaard*, [1989].

in the upper layers. Weak stability prevails below 300 m where temperature and salinity are relatively uniform. In the Greenland Sea, on the other hand, vertical stability is weak throughout the water column with pronounced thinning and even vanishing of the surface layer near the center of the cyclonic gyre (Figure 3). There surface waters are cooled in winter to become denser than the underlying water and convective overturn has been observed to depths greater than 1000 m and may even penetrate to the bottom during particularly severe winters [*GSP Group*, 1990]. The ventilation of the Greenland Sea leads to formation of North Atlantic Deep Water which contributes significantly to the

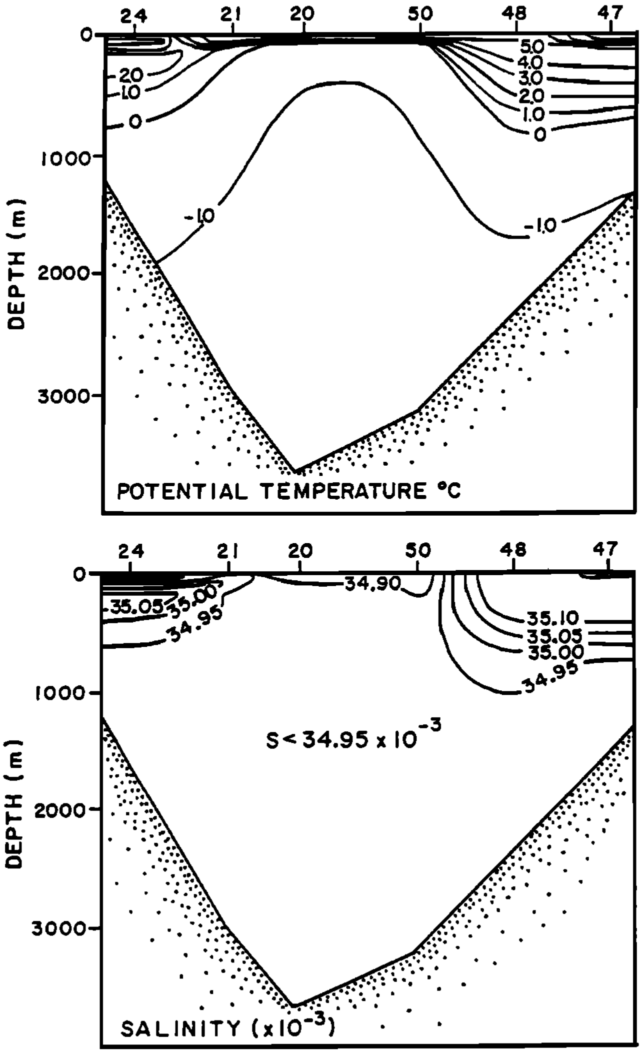

Fig. 3. Potential temperature and salinity sections extending north-northwest across the Greenland Sea [*Carmack* 1986].

global meridional transport of heat. The physical oceanography of these seas has been reviewed by *Carmack* [1986, 1990] and *Aagaard* [1989] and the physical oceanography of Fram Strait by *Hunkins* [1990]. Details of the origin, distribution, and transformation of the water masses in this region have been discussed by *Coachman and Aagaard* [1974], *Aagaard et al.* [1985], and *Rudels* [1986, 1987].

The circulation of ice and upper layers in the Arctic Ocean is driven predominately by winds. Surface circulation in the Arctic Ocean is anticyclonic, while in the Greenland Sea it is cyclonic (Figure 4). The motion of sea ice is known especially well, since it has been tracked in recent years with the aid of automatic data buoys and manned ice stations [*Colony and Thorndike*, 1984; *Colony and Rigor*, 1991]. In the Beaufort Sea, that part of the Arctic Ocean between Alaska and the north pole, mean ice motion describes a clockwise gyre, while in the region between Eurasia and the north pole the Transpolar Drift Stream is directed toward Fram Strait and then continues into the Greenland Sea with the East Greenland Current. More than 70% of the variance in ice motion within the Arctic Ocean is explained by geostrophic winds. To determine this fact, surface currents in the Arctic Ocean below the ice have been observed by two independent methods, both of which show a clockwise gyre similar to that of the ice. Using observations of geostrophic winds and ice motion, *Colony and Thorndike* [1984] estimated currents as a residual of unexplained variance, while *Coachman and Aagaard* [1974] used the density field with the assumption of negligible currents at great depth. These results show that wind maintains the ice circulation, which in turn drives the upper ocean. The mean ice drift pattern may be interrupted in late summer when the polar anticyclonic wind system weakens and even reverses. Ice drift in both the gyre and the Transpolar Drift Stream may reverse for a period of several weeks each summer [*McLaren et al.*, 1987; *Serreze et al.*, 1989]. Although there are no data yet on ocean currents during these reversals, theory indicates that the baroclinic spindown time for the upper Arctic Ocean is too long for any current change to occur during these events. The cyclonic gyre in the Greenland Sea is also driven mainly by winds, since calculations of Sverdrup transport based on observed wind data bear a quantitative resemblance to the geostrophic surface circulation determined from the density field [*Aagaard*, 1970]. The northward Sverdrup transport must be balanced by a western boundary current which constitutes part of the East Greenland Current. The Greenland gyre did not reverse itself even when the wind stress curl reversed sign for a period of 5 months.

Within Fram Strait, wind is not the principal driving force for currents beneath the ice since it has been found that the mean geostrophic current, determined as a residual from ice and wind measurements, accounts for 2 to 5 times as much mean ice motion as local wind [*Moritz and Colony*, 1988]. Flow in the strait must thus be driven by density differences between the Arctic Ocean and the Greenland Sea, and an explanation for it in these terms was provided by *Wadhams et al.* [1979] using a rotating tank experiment. When a radial barrier was introduced into a circular zonal front, the rotational constraint against meridional flow was broken and a narrow boundary current rapidly transported fresh water toward the rim of the tank in an analog of the East Greenland Current. The laboratory boundary current closely resembled the uniform potential vorticity model calculated by *Manley et al.* [1987*a*] on the basis of the section shown in Figure 5. In that model the exponential profiles for interface depth and velocity have e-folding widths scaled by the internal radius of deformation (9.4 km for their data). Using this and appropriate values for other parameters they found a volume transport for the East Greenland Current of $1.1\times10^6$ m$^3$ s$^{-1}$, which compares well with the value of $0.9\times10^6$ m$^3$ s$^{-1}$ found by *Rudels* [1987] on the basis of budget calculations although it is much less than the result of $3\times10^6$ m$^3$ s$^{-1}$ arrived at from moored current measurements by *Foldvik et al.* [1988]. On the eastern side of the strait the ice-free West Spitsbergen Current carries warmer, more saline water north into the Arctic Ocean along the surface to a latitude of about 81°N, where it descends to become a subsurface current. Mean surface winds and hence ice stresses on the water are directed toward the southwest across the entire strait, so the West Spitsbergen Current flows against the wind and thus must also be driven by buoyancy forces. Note that wind stresses at coastal stations are not a reliable indicator of stresses over the strait. Recent data on winds in the Fram Strait region are summarized by *Jonsson* [1989], and pressure data are summarized by *Colony and Rigor* [1991]. These observations and ideas agree with the concept of the Arctic Ocean as an estuary of the Atlantic Ocean with saline inflow at depth and fresh outflow at the surface. Since Fram Strait is very wide, rotational effects

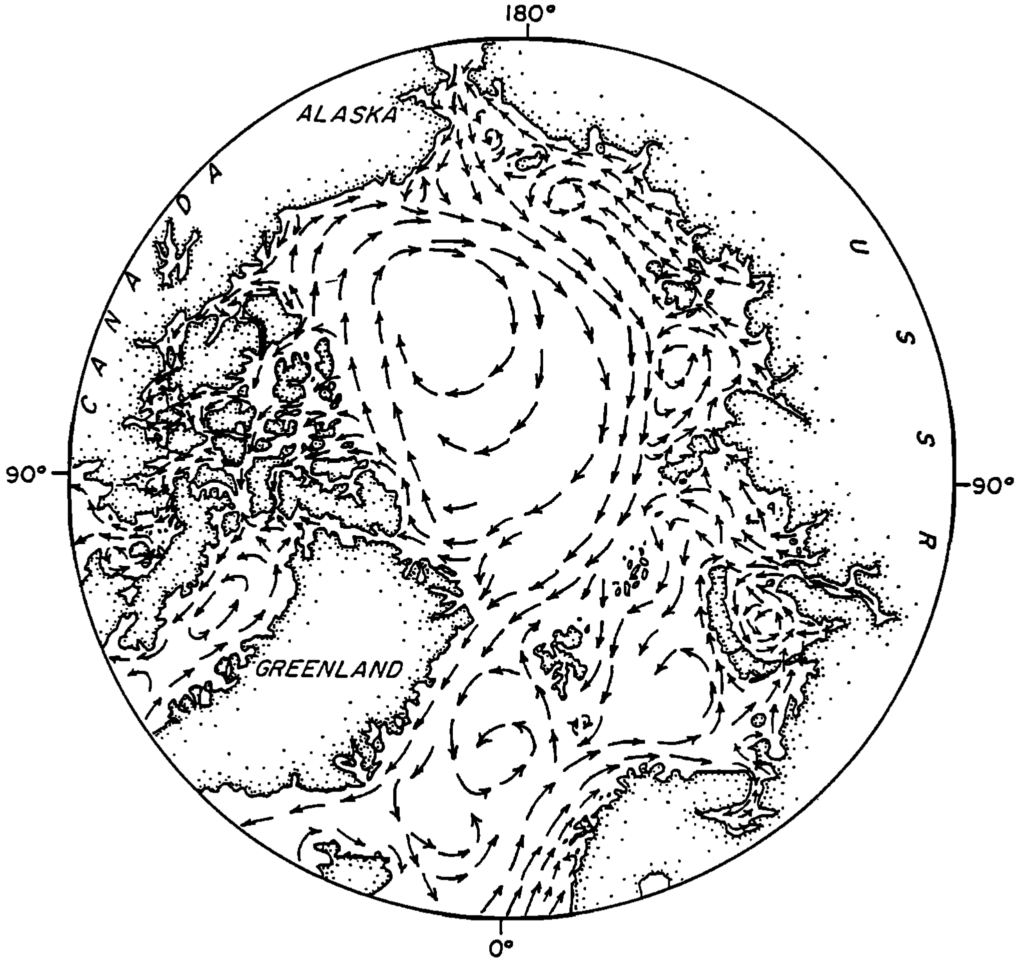

Fig. 4. Schematic surface circulation of the Arctic Ocean and Greenland Sea, Redrawn from Tchernia [1980].

are important and the front between the two water masses is inclined across the strait. This is most evident in the East Greenland Current where the front slopes upward from west to east. In the section shown in Figure 5 the interface as defined by the 0°C isotherm slopes upward from 180 m on the western edge of the section to intersect the surface at a location 80 km to the east.

A number of analytical and numerical models have been presented to explain various aspects of the circulation in the Arctic Ocean, the Greenland Sea and Fram Strait. A two-layer geostrophic model of Arctic Ocean circulation based on estuarine research has been developed by *Stigebrandt* [1981] in which ice and an upper layer freshened by runoff and precipitation flow out while a deep Atlantic layer of higher salinity flows in through Fram Strait. Entrainment of the lower layer into the upper produces a balanced exchange. A modified version of this model has been compared by *Rudels* [1989] with an alternative model of his in which the mixing of the lower layer into the upper is accomplished by shelf processes rather than by entrainment. He finds that shelf processes appear to dominate at the present time. Considerable effort has been devoted to numerical modeling of polar and subpolar seas and approaches have involved one-, two-, and three-dimensional configurations with various formulations for ice behavior. A numerical model of air-sea-ice circulation which includes ice dynamics as well as time dependence has been used by *Semtner* [1987] to predict ice coverage using observed mean monthly atmospheric forcing and a prescribed inflow through the Faeroe-Shetland Channel. This model evolves into a two-layer exchange after a 20-year integration, but published results focus more on ice coverage than on currents. This model was also used to study interannual ocean forcing of the ice pack [*Fleming and Semtner*, 1991]. Another numerical model with extensive ice dynamics is that of *Hibler and Bryan* [1987], which differs from the previous one in being diagnostically constrained to remain close to observed values of temperature and salinity on a 3-year time scale. A third three-dimensional numerical model of the Arctic Ocean and Greenland Sea which reproduces many of the observed features is that of *Piacsek et al.* [1991]. A simpler numerical model has been developed by *Wood and Mysak* [1989] which covers only the Greenland Sea. In their model, Sverdrup transport toward the north in the central and eastern ice-free areas is matched on the western side with a southward coastal boundary current, the East Greenland Current, which is based on an analytical solution given by *Gill* [1982] to the problem of the flow in a channel after removal of a dam.

In this paper we approach the question of the flow through Fram Strait by observing flows in laboratory models and discussing theoretical implications of these flows. Experiments in buoyancy-driven exchange (section 2) produce a qualitative picture that resembles the flow in Fram Strait. These suggestive observations do not answer the question as to

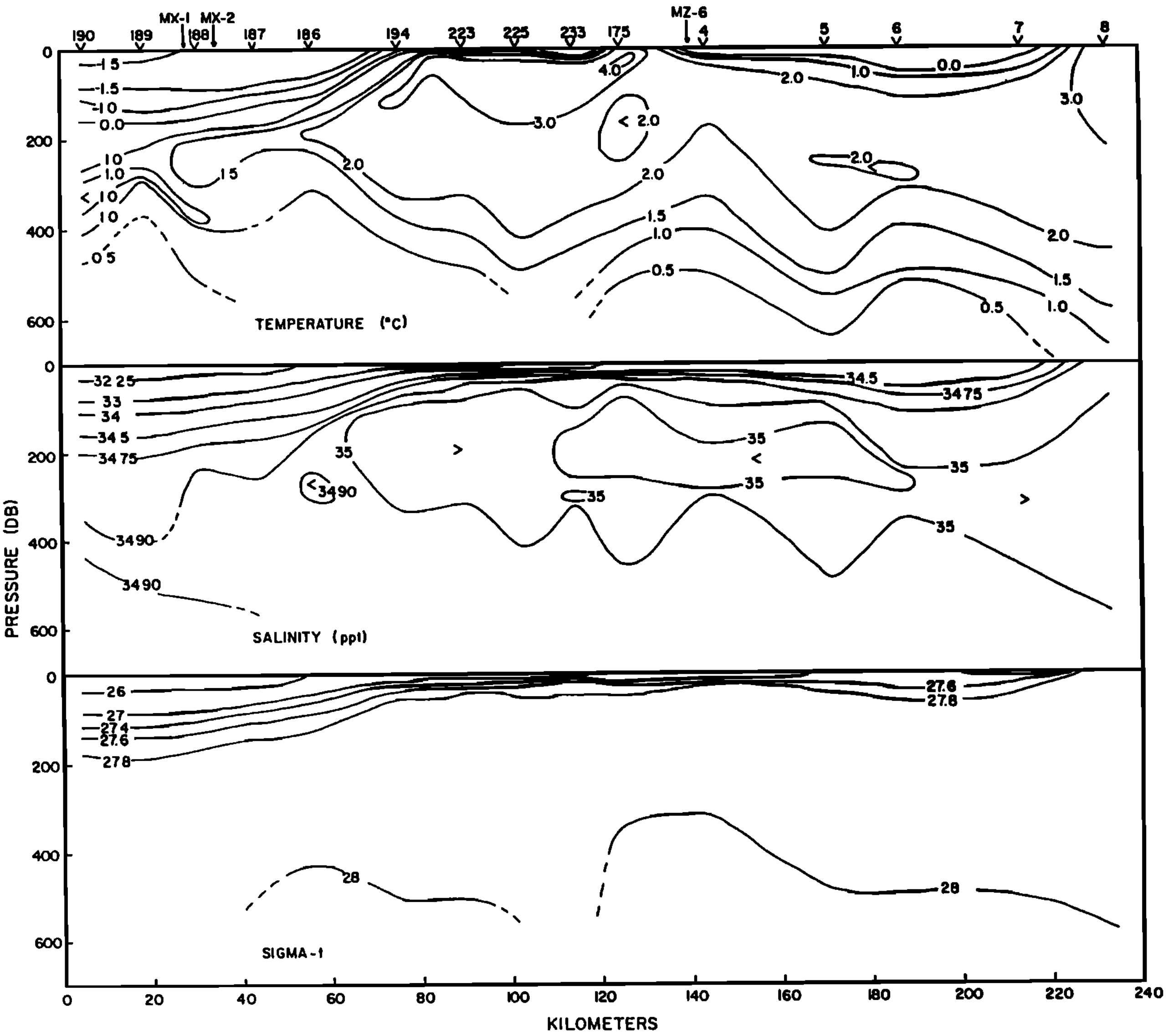

Fig. 5. Temperature, salinity and density ($\sigma_t$) sections across Fram Strait at 79°north extending from 60°W to 40°E [*Manley et al.*, 1987a].

why Fram Strait happens to be the location where different water masses are separated. Wind-driven experiments and theory (section 3) show that wind ($f$– plane dynamics) will drive fresh water into the Arctic Ocean rather than allow it to leave. A quantitative lock-exchange theory is produced in section 4 that predicts the magnitude of flux as a function of depth and density of the low-salinity layer in the Arctic Ocean. This theory is tested by laboratory experiments in section 5, and implications to the freshwater balance of the Arctic Ocean are calculated in section 6. Concluding remarks are made in section 7.

## Buoyancy-Driven Exchange

Laboratory experiments were conducted to observe the flow patterns in density-driven rotating "lock-exchange" experiments, where water with one density flows from its original basin through an opening into a second basin after a sliding gate separating the two fluids is removed. Likewise, the water of different density in the second basin flows back into the first basin. The intent was to observe the size and location of the currents for various values of density difference, rotation rate, and assorted sidewall geometries with varying degrees of resemblance to Fram Strait. The hope is that comparison of the flow patterns with the flows known to exist in Fram Strait will enable one to more clearly understand the dynamical origin of some of the currents in Fram Strait.

In all experiments, there was a layer of deep salty water with the dynamically active shallow layers above them. This deep layer represents the deeper water in the Fram Strait regions, below approximately 300 m depth. The shallow layers represent surface waters in the Arctic Ocean for the first basin and the Norwegian-Greenland Sea for the other basin. These layers serve as the source waters for the East Greenland Current and the West Spitsbergen Current, respectively. In order to make the situation as simple as possible, no attempt is made to incorporate the important deeper currents in Fram Strait. These do have important oceanic volume and salinity fluxes but they are slower and associated with smaller pressures than the surface currents.

Four experimental configurations were employed as sketched in Figure 6. The first two shared the same container geometry. A 1.06-m-diameter cylindrical container was mounted on a rotating turntable, and two false peninsulas were constructed so that the cylinder had two basins joined by a strait 40.5 cm wide. The configuration was intended to geometrically model the Arctic Ocean, Fram Strait, and the Greenland-Norwegian Sea. In the first configuration, there was a layer of fresh water in one basin and none in the other. In the second there were surface layers in each basin of differing density. The third and fourth configurations employed tanks of different geometries. In the third, a rectangular tank 183 cm long, 19.2 cm wide, and 24.8 cm deep was used so that some of the possible effects from curvature of the sidewalls could be eliminated. The sliding gate was inserted perpendicular to and midway along the long axis of the tank. This resulted in a strait as wide as the two equally sized upstream basins. In the fourth configuration, a 2-m basin was divided along a central cord by a sliding gate that was removed to start the experiment. This last configuration was expressly intended to produce the largest possible hydrostatic number in order to resolve whether eddies and slow velocities observed in the earlier runs were produced by a small hydrostatic number.

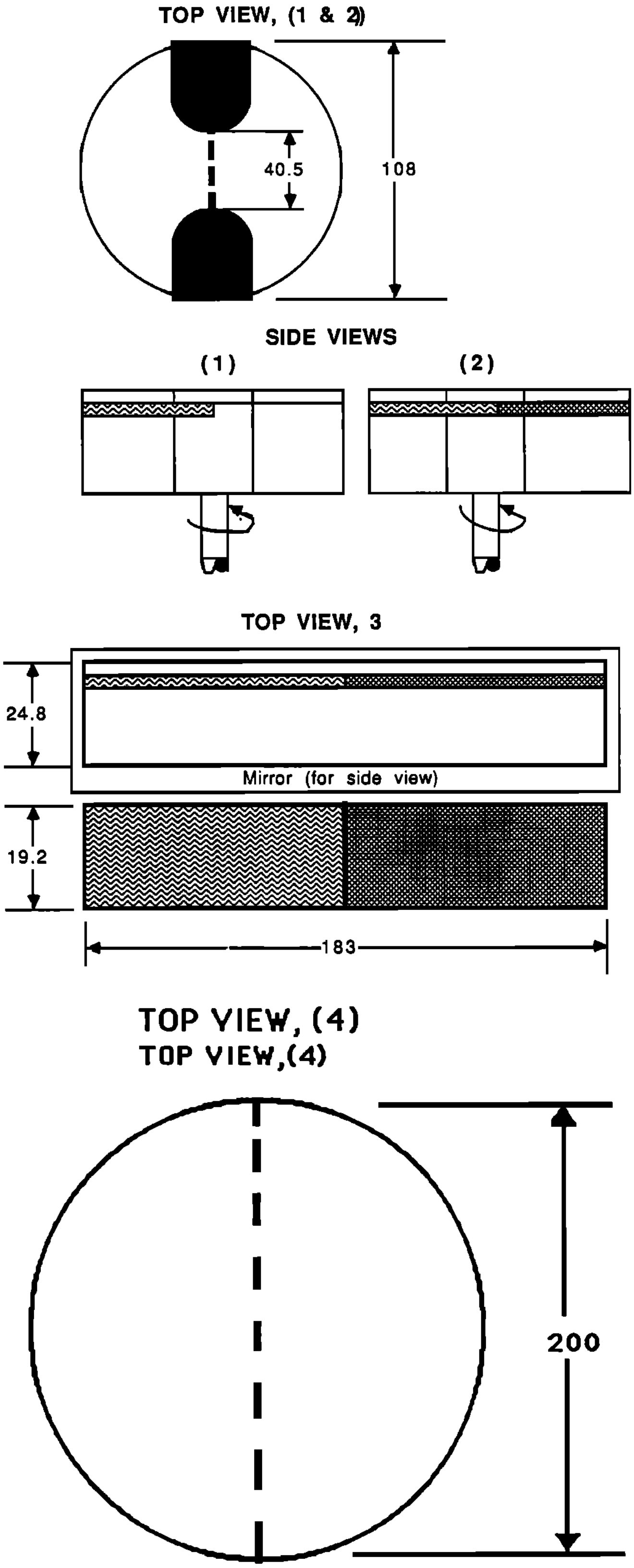

Fig. 6. Sketch and dimensions of the four experimental apparatuses. All photographs are oriented so the equivalent of the Arctic Ocean is at the top.

Scaling considerations produce seven dimensionless numbers: There are ten independent variables in the experiments (except for the first that had nine): gravity $g$ = 980 cm s$^{-2}$, depth of the shallow layers $h_1$ = 5 cm and of the deep layer $h_2$ = 20 cm (in a few cases we had to resort to 18 cm because of geometrical constraints), Coriolis parameter $f = 4\pi/T$ where $T$ is period of rotation of the tank, ($f$ was varied from 0.2 s$^{-1}$ to 1.7 s$^{-1}$), kinematic viscosity of the water $\nu$ = 0.01 cm$^2$ s$^{-1}$, density of the two surface layers $\rho_1$ = 0.998 g cm$^{-3}$ and $\rho_2$ = 1.000 g cm$^{-3}$ (not present in the first configuration) and of the deep layer $\rho_3$ = 1.002 g cm$^{-3}$, the width of the gate $L_1$ and finally the width of the basins $L_2$. Since there are three dimensional units of mass, length, and time, seven (six for the first) dimensionless numbers result. Each of these will now be discussed.

*Dimensionless number 1: Depth of the bottom fluid.* This is given by the ratio of shallow layer to deep depth $h_1/h_2$ which is 0.25. This being less than 1 implies that dynamics of the bottom fluid should be less important than the dynamics of the surface layers, but it is not clear that the deep layer can be completely ignored. Some experiments will show that the surface jets possess the dynamics that jets are believed to have when they lie over infinitely deep fluid.

*Dimensionless number 2: Friction.* The Ekman number of the bottom fluid. $E = \nu/fh_2^2$ is $10^{-4}$ so the usual Ekman layers will be found on the bottom. We note that Ekman number of the shallow layers is going to be expressed as the above Ekman number divided by the square of the depth ratio. This dimensionless number is 16 times larger than the Ekman number of the deep fluid so there should be slight viscous coupling between the layers. Unfortunately, the physics of that coupling is poorly understood. Spin-up time estimates will be given later to indicate that viscous forces are smaller than inertial forces in the experiments.

*Dimensionless number 3: The Boussinesq approximation.* The density difference between the fluids is fixed at 0.002 g cm$^{-3}$ and 0.004 g cm$^{-3}$ for all experiments and is small compared to the absolute values of the density. Therefore, the Boussinesq approximation should be valid.

*Dimensionless number 4: Width of the gate.* The ratio of the width of the gate to the Rossby radius of deformation based upon density difference between the two top fluids.

This is written as $W = fL_1/[gh_1\rho_1 - \rho_2)/\rho_3]^{1/2}$ and is inversely proportioned to the square root of the Burger number. It may be as large as 20 for Fram Strait and is varied in the experiments.

*Dimensionless number 5: Steepness of the front between the two upper fluids.* This is not necessary for the first configuration. It is given by the ratio of the Rossby radius based upon density difference between the two top fluids to the Rossby radius based upon density difference between the fresh and bottom fluids. In all experiments this is $2^{1/2}$.

*Dimensionless number 6: Width of the Rossby radius based upon density difference between the two top fluids compared with the depth of the upper layer.* We call this a hydrostatic number $H_y = [g(\rho_1 - \rho_2)/h_1\rho_3]^{1/2}/f$. To derive shallow water equations, this must be large, and it is almost always large in the ocean. $H_y$ is varied in the experiment. In experiments 1 through 3, $H_y$ spans the range 4 to 0.5. Experimental configuration 4 was constructed to make both $H_y$ and $W$ large together.

*Dimensionless number 7: Ratio between gate width and a dimension of the basin, $L_1/L_2$.* This number is varied in the experiments. In order to attain a flow that is representative of a steady flow, we try to make this as large as possible.

Dimensionless numbers 1, 3, and 5 are fixed for all the experiments described in the next section. The others will be given where appropriate.

### *Qualitative Results*

In the first configuration, 20 cm of salt water was added to the tank and spun up to a counterclockwise rotation with a period of 15 s ($f = 0.84$ s$^{-1}$). A watertight sliding gate was then inserted across the strait down to a depth of 8 cm, and 5 cm of fresh water was slowly added to the top of one basin, resulting in a water depth below the layer $h_3$ of 17.5 cm. The run commenced when the gate was raised. Three runs were conducted with increasing $f$ and therefore increasing $W$ and decreasing $H_y$.

The front adjusted gravitationally in approximately the first rotation period to develop into a rotational density current. As is shown in Figure 7, the fresh water began to flow toward the other basin by turning to the right looking from the fresh water basin toward the other one. It flowed along the front until it hit the right hand wall. At that point, a density current with a "nose" similar to that observed by *Stern, et al.* [1982], and *Griffiths and Hopfinger* [1983] was observed to emerge from the front and move along the right hand wall away from the layer of fresh water. The sequence of photographs in Figure 7 shows the front between the two waters after 22 s. The density current extending into the clear basin is the principal mechanism for transporting fresh water far into the second basin.

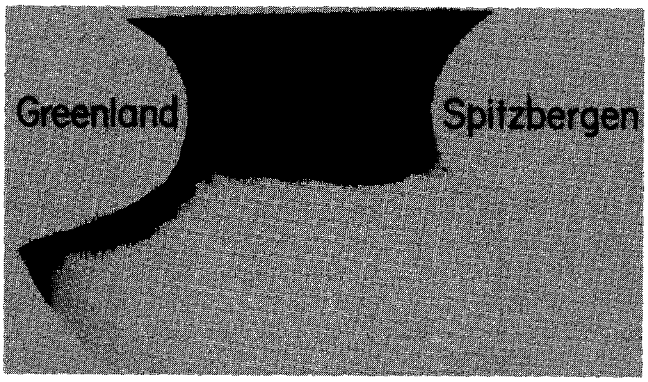

Fig. 7. Top view of dye spreading in the first configuration where there is a layer of fresh water dyed black 5 cm deep in one basin over 17.2-cm-deep salt water. There is 22.5-cm-deep clear salt water in the second basin . Time of the photograph is 22 s after removal of the gate.

Back at the gate region, something else of interest was happening at the other end of the front, where it intersected the left-hand wall. Fresh water was fed into the front by a current in the upstream basin that flowed along the left-hand wall. At the point where this water fed into the front, there was some inertial "overshoot" of the fresh water similar to that calculated by *Hermann et al.* [1989]. The overshoot produced a meander that gradually caused the left-hand point where the front touched the wall to move downstream, and in fact the entire meander migrated slowly into the second basin. As time progressed, the meander became larger, and by the time the nose had circled the downstream basin, the meander was quite sizeable. The migration of this meander was slower than the propagation of the nose along the other wall, but the volume of the fluid within the meander was larger. Therefore although the density current on the right-hand wall is the principal mechanism for moving fluid far into the second basin, the meander can move greater volumes of fluid small distances into the second basin. The meander process can potentially confuse measurements within the strait that attempt to measure volume flux from the fresh water basin into the other basin. This process was observed for all three values of $W$ and $H_y$.

The first configuration demonstrated the existence of the bore and the development of a meander at the mouth that is associated with overshoot of the fluid flowing along the left-hand wall. Both processes have been studied previously. This also provides a comparison with the second configuration, which was felt to be a closer approximation to the situation in Fram Strait. In this configuration, 5.2-cm-deep layers of water with differing densities were placed in both basins. The lightest water was fresh water and the intermediate water had a density midway between the fresh water and the deep water (whose depth was again 20 cm). After the tank was spun up, the gate was removed. A front formed within one rotation period as it had in the first run, but significant qualitative differences from the flow in the first configuration were soon apparent:

The greatest difference (Figure 8) was that two density currents moved in opposite directions from the points where the front intersected the sidewalls. Each density current was found in its respective right-hand wall looking from its basin to the other one. The freshwater current flowed out over the top of the intermediate water. The nose appeared to be similar to the laminar noses in the first configuration. The intermediate water current had a nose that wedged between the fresh water and the deep water. The nose of this density current looked more laminar and smaller than the nose of the one layer problem.

Second, there was a region of pronounced overshoot of both of the currents coming out of the basins on their respective left-hand walls. That region was bigger than previously seen and essentially resembled overshoot observed in numerical experiments [*Hermann et al.*, 1989]. Here the region of overshoot was clearly found to be more unstable than in the numerical experiments. The overshoot sometimes de-

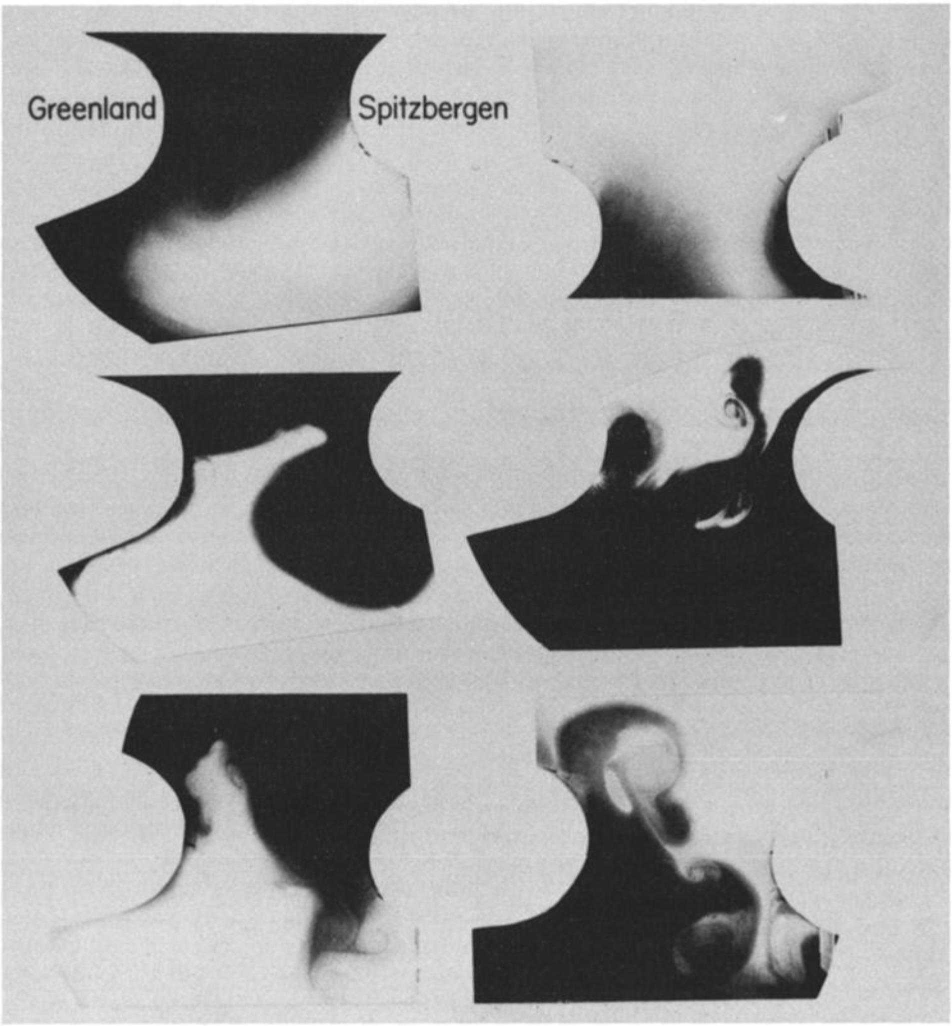

Fig. 8. Top views of dye spreading in the second configuration after approximately 60 s. Photographs show dyed freshwater experiments on the left and dyed saltwater experiments on the right. Values of $W$ for each pair are 5.3, 10, and 22 from top to bottom.

veloped a dipole eddy structure shown in the photographs in Figure 8. The dipole indicates that there is considerably more dynamic (baroclinic) coupling between the two layers than there was between the one layer and the deep fluid in run 1. Finally, more eddies were produced along the front and these seemed to also have a dipole character.

For the third configuration, parameters were similar to the corresponding runs in the second, so a close comparison of the effects of curving versus straight sidewalls could be made. Photographs at roughly the same times as Figure 8 are shown in Figure 9. The wall jets appeared to be approximately the same shape and strength as in case 2. The overshoot on the left-hand walls is much less, but the eddies are more pronounced, especially those coming off the density current that moves out of the freshwater basin. There is a clear impression that the curvature of the walls is very important to both overshoot and instability processes for these currents.

The purpose of the fourth configuration was to observe experiments with the same $H_y$ as before but to have larger $W$ than before. For this configuration, the rotation rate and density difference were similar to the corresponding runs in the second and third, so a close comparison could be made. Photographs at roughly the same times as Figures 8 and 9 are shown in Figures 10 and 11. As before, the wall jets appeared to be approximately the same shape and strength as in case 2. The eddies in the front between the two lateral walls have much more space to develop, but they develop much less vigorously than in the preceding cases. This can be attributed to a jet that is apparently less throttled by a narrow opening. The overshoot on the left-hand walls is about the same as in the third case. There is a clear impression that the surface wall jet speed still scales with the gravity wave speed but the internal wall jet propagated more slowly.

### *Quantitative Results*

Velocity of the noses of the intruding currents was estimated from the experimental results by measuring the distance traversed during one time interval. In the second configuration photographs were not taken frequently enough to determine in detail whether the noses were changing their speed during the experiment, so efforts were made to determine the velocity as early in the run as possible. The velocity measurements should be regarded as having relatively large errors, of the order of tens of percent or more. In the third configuration, the trajectories of the noses are shown in Figure 12 and 13 and velocities were obtained from

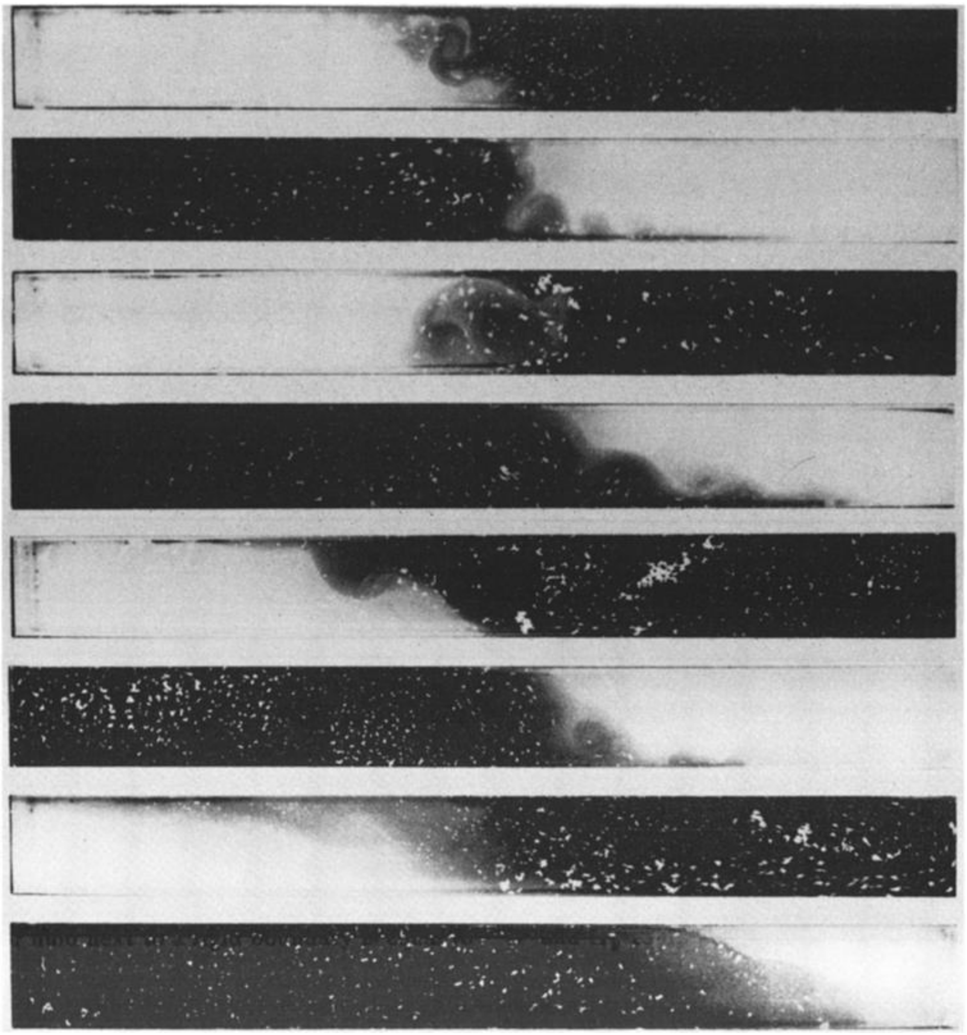

Fig. 9. Top views of dye spreading in the third configuration after approximately 60 s. Starting from the left the photographs show successively dyed freshwater and then dyed saltwater experiments that have the same value of $W$. Pairs of photographs have values of W of 1.2, 2.5, 5, and 10 from left to right.

the calculated slope of the rms best fit lines shown. All velocities are given in Table 1 along with rotation periods $T$, strait and basin widths $L_1$ and $L_2$, and Rossby radius based on the density difference between the two upper fluids $R = [g\ (\rho_1 - \rho_2)\ h_1/\rho_3]^{1/2}/f$. Averages of the velocity data were taken down the columns as well as across the rows. They reveal that velocity decreased systematically with increasing rotation rate and that the freshwater nose went faster than the intermediate water nose. Dimensionless numbers are shown in Table 2 where those velocities were divided by wave speed $(g'h_1)^{1/2}$, where $g' = g(\rho_3 - \rho_1)/\rho_3$. We note that as rotation rate is increased, the Rossby radius is systematically reduced, the Ekman number is also decreased, the hydrostatic number $H_y$ decreases from greater than to less than 1, and the ratio $W$ of width of the tank to Rossby radius becomes progressively greater. From the experimental measurement in Table 1 of a systematic decrease in nose velocity alone it is not clear whether the decrease in velocity and the tendency for more eddies is determined by a decrease in $E$, a decrease in $H_y$, or an increase in $W$.

The following considerations indicate that Ekman friction is probably negligible for these experiments. The Ekman spindown time for fluid next to a rigid boundary is equal to $\tau = d/(\nu f)^{1/2}$. If we take $d = 5$ cm, $\nu = 0.01$ cm $^2$ s$^{-1}$, and $f = 1.7$ (the largest value), then $\tau = 38$ s. But the top layer could probably not spin down this rapidly. There is no rigid boundary at the top of the top layer, and force would have to be transmitted to the bottom fluid. Although the transmission of drag through density interfaces is poorly understood, it is believed that spin down time between the top fluid and the bottom fluid, i.e., between two fluids of different salinity, would be much larger than this value. It is known [*McDonald and Dicke*, 1967] that stratification greatly inhibits spindown. Also, the spindown time of the bottom layer would be 4 times this value. In addition velocity showed little decrease with time in Figures 12 and 13. Sidewall friction is not well understood, and its role in the density currents is less certain. Its effect was ignored in previous studies by *Stern et al.* [1982] and *Griffiths and Hopfinger* [1983].

In spite of the small friction, the noses were observed to slow down significantly with increasing rotation, and there were also more eddies observed. We wondered whether the slowing down of the nose speed and the increased eddy activity is determined by a decrease in $H_y$ or by an increase in $W$. The fourth experiment had different relative values of $W$ and $H_y$ compared with the third, so one could get some

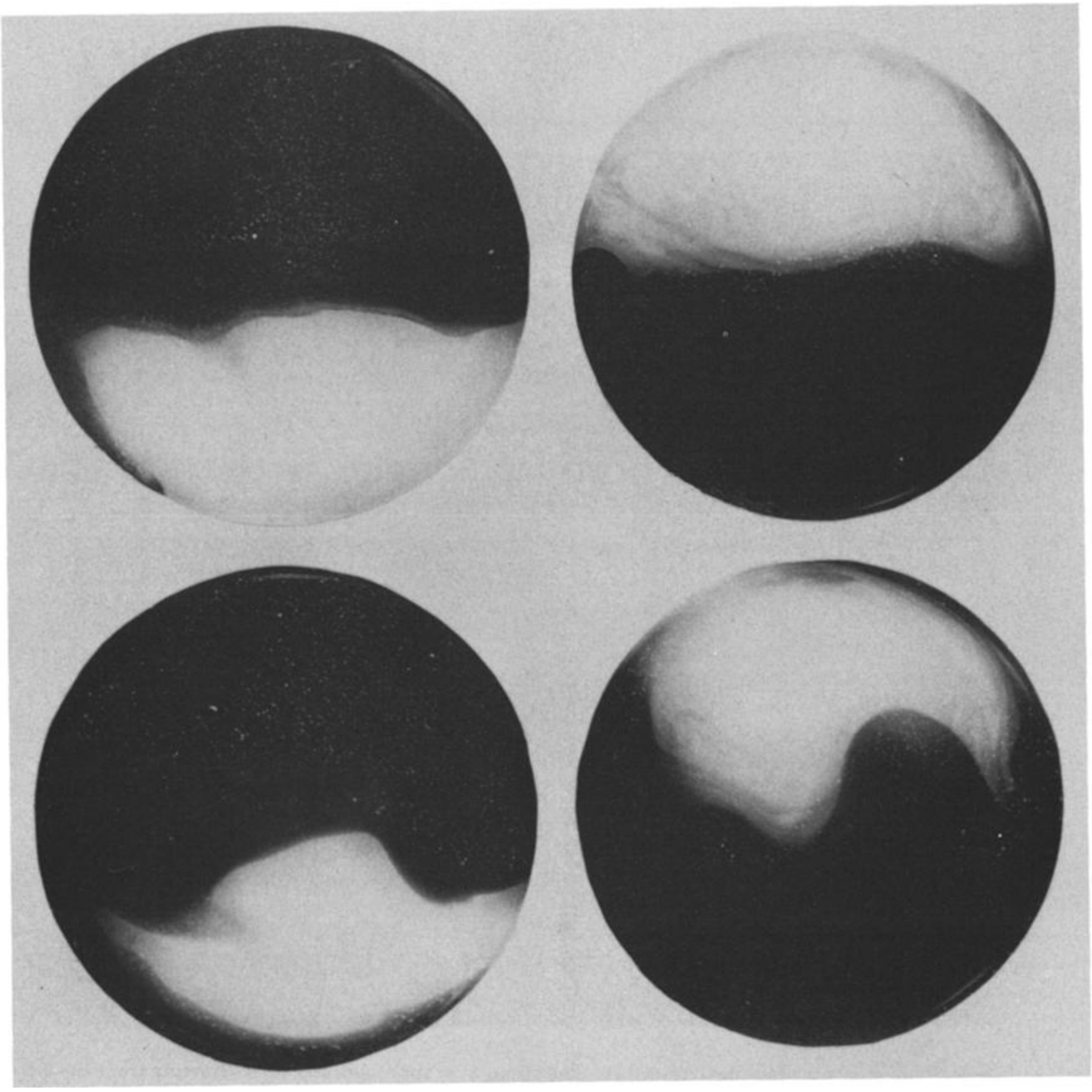

Fig. 10. Top view of dye spreading in the fourth configuration for $W = 10$. (Left), Freshwater dyed, $t =$ (top) 45 s , and (bottom) 121 s. (Right), Salt water dyed, $t =$(top) 92 s, and (bottom) 210s.

indication of the answer by comparing the results. Unfortunately the comparison was not conclusive. For 60 s the intermediate nose had significantly slower nose speed for larger $W$ (in configuration 4 as compared to configuration 3), but the same was not true for 30 s. Conversely, for 30 s the top nose had faster speed with larger $W$. Eddy activity seemed to be less with larger $W$, but this result is subjective.

In summary, the density-driven flows can get set up as a steady feature in spite of the transient nature of the experiment. The nose velocities are very steady, especially when $H_y$ and $W$ are large. Surface nose velocity scales as $(g'h)^{1/2}$ for $W$ and $H_y$ large. Intermediate nose velocity exhibits a less distinct correlation with $(g'h)^{1/2}$. In some cases it exhibited a significantly smaller velocity than the top nose; this may be the result of some dead water effect. Unfortunately scatter for the intermediate nose velocity was very large, and the resolution of the dependence of it on the external parameters is beyond the scope of this study. No stationary front is found at the mouth. Eddies are plentiful (baroclinic instability?) on the basis of these observations the front would be expected to twist, undulate, and shed eddies perhaps forever. Significant eddies are produced for small $H_y$ but less so for larger $H_y$ and $W$. The Hermann-Rhines-Johnson overshoot [*Hermann et al.*, 1989] on the left side of the strait looking downstream was widely observed, but it did not apparently lead to a large transport far from the opening. The density current on the right wall remains as the location of greatest transport far from the opening.

## WIND-DRIVEN EXCHANGE

The experiments on buoyancy-driven exchange previously described were motivated by the observation that circulation of the upper layers within Fram Strait is evidently not forced by wind and ice stress. However since large-scale circulation of the upper layers in both the Arctic Ocean and the Greenland Sea is observed to be strongly (even primarily) wind-driven it is possible that exchange through the strait may be forced by pressure gradients arising from remote winds. Experiments were run to study the motion of a surface layer in a divided basin with wind forcing. The tank used in these runs had an inside diameter of 45 cm and a height of 30 cm and was divided along a diameter into two semi circular basins by a wall with a gap of 10 cm in the middle (Figure 14). A saline layer 18 cm deep was first introduced into the tank and spun up to solid rotation. Next,

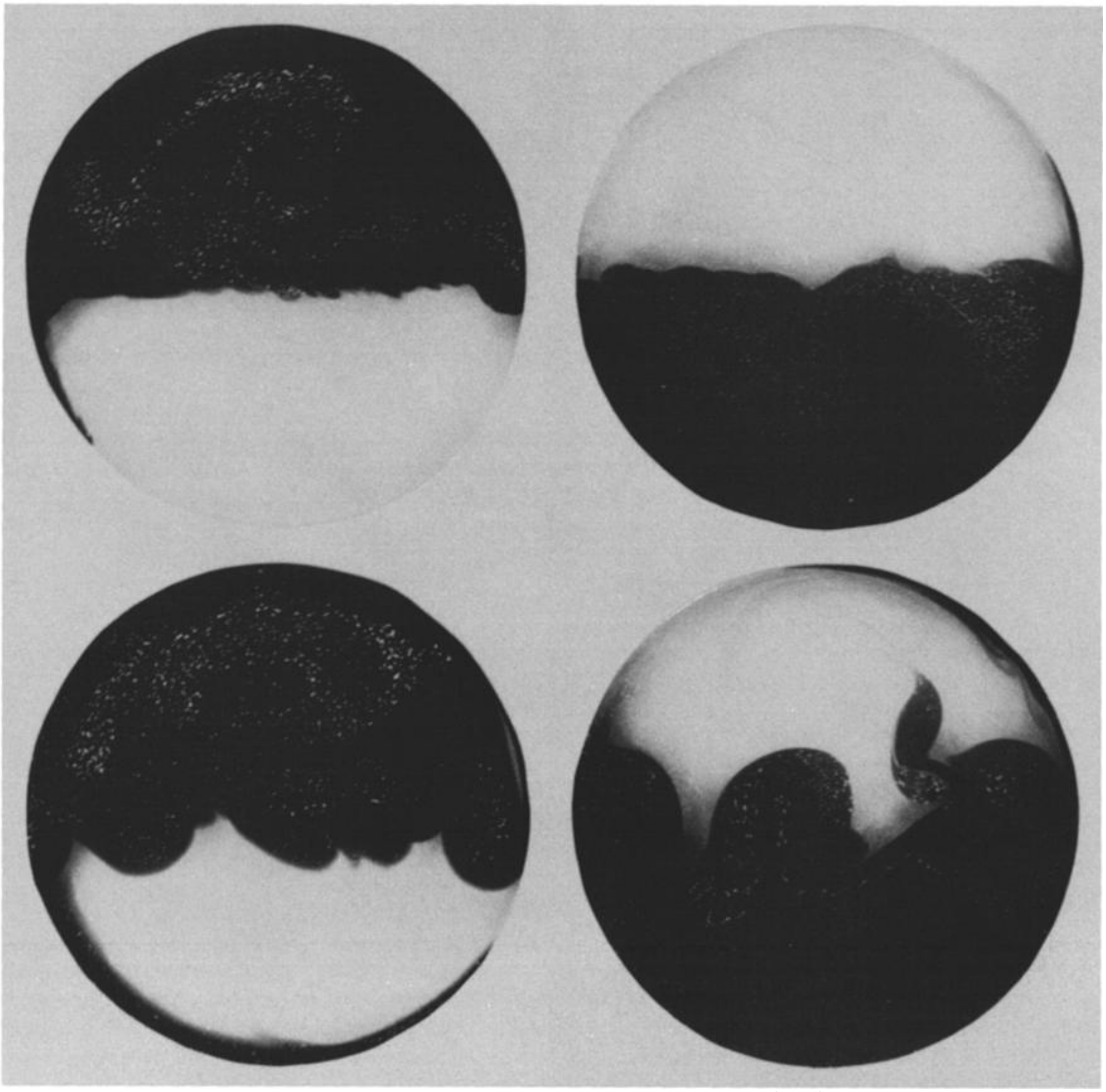

Fig. 11. Top view of dye spreading in the fourth configuration for $W = 20$. (Left), Freshwater dyed is shown at a time of (top) 46 s and (bottom) 157 s. (Right), Salt water dyed is shown at a time of (top) 60 s and (bottom) 240 s.

a freshwater layer was carefully floated onto the surface of both basins. No gate was used, and there was no initial pressure difference between the two basins. In the absence of wind there would have been no exchange. The tank was rotated at a rate of 0.25 revolutions per second for all runs. The upper layer was 1.2 cm deep , much less than the lower layer depth, so these runs corresponded to reduced gravity dynamics on an $f$-plane.

A small turbine blower mounted on the tank directed an air stream parallel to the wall in a well-defined jet with a width of about 10 cm. The axis of the jet corresponded with the wall diameter, so wind shear was of opposite sign in the two basins. Using an idealized global surface wind system as a conceptual model, this setup bears some resemblance to the stress on the Arctic Ocean and Greenland Sea (Figure 15) although the actual center of the polar gyre is displaced from the north pole to the center of the Arctic Ocean [*Colony and Rigor*, 1991]. It is through the ice- pack that wind stress is transmitted to the Arctic Ocean, and as we noted in the introduction, pack ice describes an anticyclonic gyre in this ocean. Mean ice vorticity in the Arctic Ocean, and hence ice stress curl exerted on the water, is negative (R. Colony, private communication, 1990). In the Greenland Sea, on the other hand, the wind stress curl is positive [*Jonsson*, 1991], since this sea is located in the shear between the polar easterlies and the zonal westerlies. Wind stress curl vanished in the model at the gap, thus simulating Fram Strait, where the curl of the mean wind stress is nearly zero. Dimensional parameters for this experiment are presented in Table 3 where they are compared with corresponding values for the Arctic Ocean and Greenland Sea. Dimensionless parameters derived from these values are shown in Table 4. As in the earlier experiments there is fairly good correspondence between the ocean and laboratory values for Rossby and Ekman numbers. The laboratory value for Burger number $S$ is larger than the oceanic value but still less than 1 as desired. The hydrostatic number $H$ is only slightly larger than 1 in the model, and therefore hydrostatic conditions may not always prevail. The vertical geometric ratios are similar for ocean and model, but the horizontal ratio is much larger in the model than it is in the ocean. A much larger tank than was practically possible would have been necessary to obtain better agreement for this ratio.

Soon after the blower was started the dyed upper layer began to flow through the gap from the "subpolar" to the "polar" basin, where after a few rotations a circular anti-

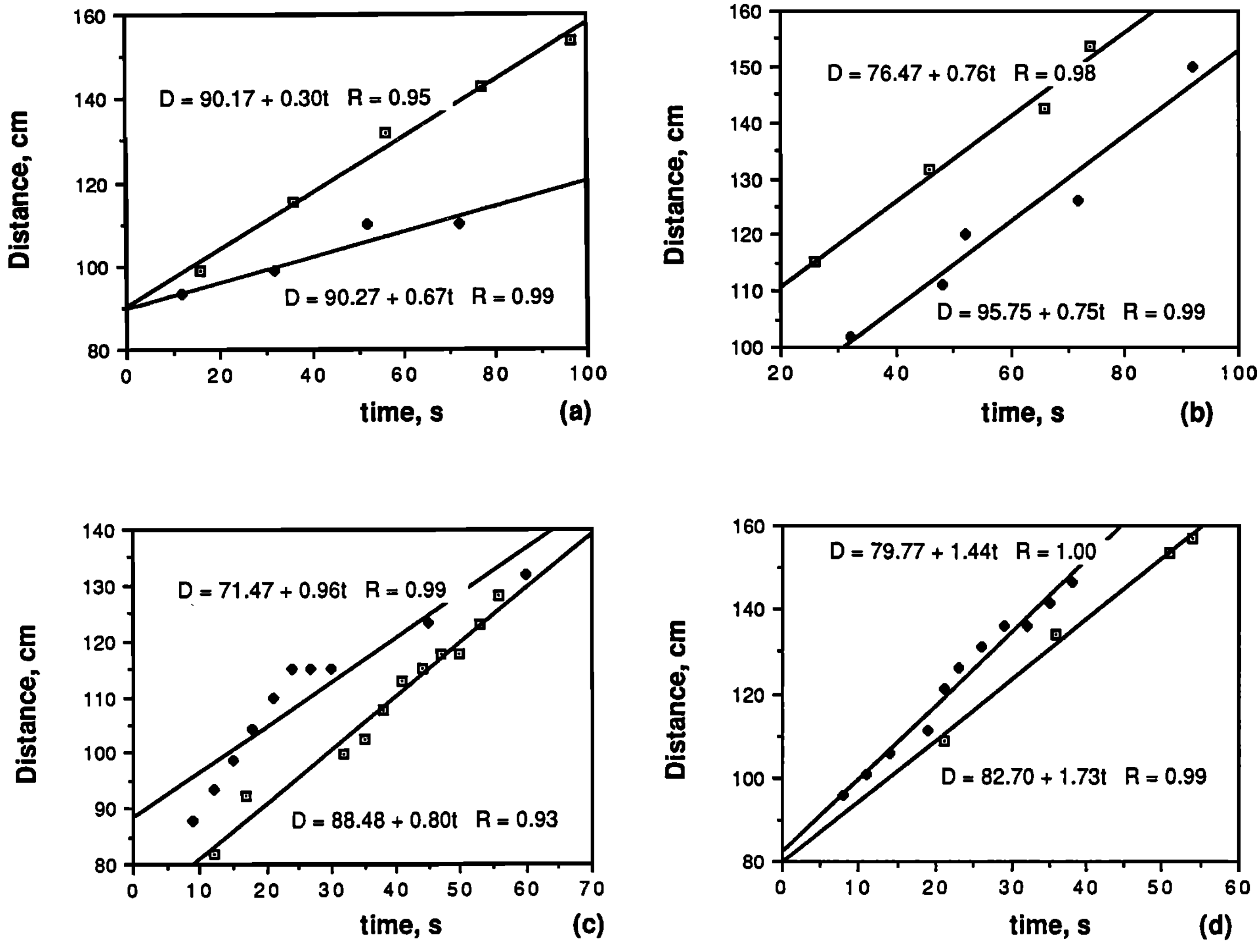

Fig. 12. Trajectories of the noses for the configuration 3 runs. Periods of rotation are, (*a*) 7.5, (6) 30, (e) 15 and (d) 60 s. The squares are for the freshwater nose and the diamonds are for the intermediate water nose.

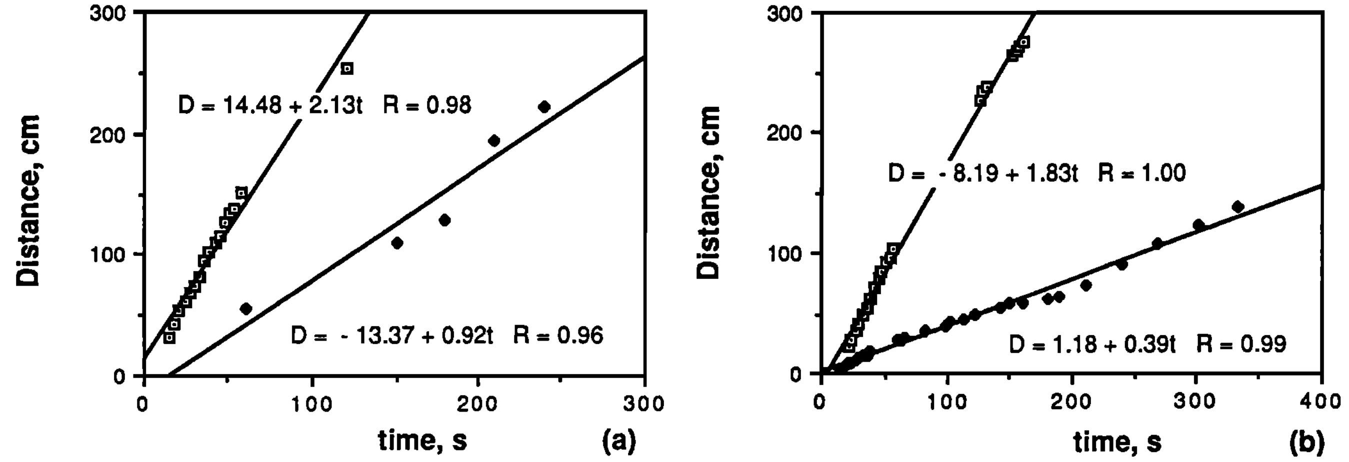

Fig. 13. Trajectories of the noses for the configuration 4 runs. Periods of rotation are, (*a*) 30 and (*b*) 60 s. The squares are for the freshwater nose and the diamonds are for the intermediate water nose.

TABLE 1. Velocity Measurements of Buoyancy-Driven Experiments

| Config. # | T s | R cm | $L_1$ cm | $L_2$ cm | $V_f$ cm $s^{-1}$ | $V_i$ cm $s^{-1}$ | $V_{Avg}$ cm $s^{-1}$ |
|---|---|---|---|---|---|---|---|
| 1 | 15 | 5.0 | 40.5 | 107 | 2.3 |  | none |
| 2 | 30 | 7.8 | 40.5 | 107 | 1.6 | 1.1 | 1.35 |
| 2 | 15 | 4.1 | 40.5 | 107 | 1.2 | 0.9 | 1.05 |
| 2 | 7.5 | 1.9 | 40.5 | 107 | 0.8 | 0.3 | 0.55 |
| 3 | 60 | 16 | 19.2 | 91.5 | 1.44 | 1.73 | 1.59 |
| 3 | 30 | 7.8 | 19.2 | 91.5 | 0.96 | 0.80 | 0.89 |
| 3 | 15 | 4.1 | 19.2 | 91.5 | 0.75 | 0.76 | 0.76 |
| 3 | 7.5 | 1.9 | 19.2 | 91.5 | 0.67 | 0.30 | 0.49 |
| 4 | 60 | 16 | 200 | 100 | 1.83 | 0.39 | 1.14 |
| 4 | 30 | 7.8 | 200 | 100 | 2.13 | 0.92 | 1.52 |
| Average |  |  |  |  | 1.27 | 0.80 |  |

TABLE 2. Dimensionless Numbers for the Buoyancy-Driven Experiments

| Config. | $E$ | $W$ | $H_y$ | $V_f/\sqrt{g'h_1}$ | $V_i/\sqrt{g'h_1}$ | $L_1/L_2$ |
|---|---|---|---|---|---|---|
| 1 | $3\times10^{-5}$ | 0.1 | 1 | 0.6 | none | 0.38 |
| 2 | $6\times10^{-5}$ | 5.3 | 1.6 | 0.49 | 0.34 | 0.38 |
| 2 | $3\times10^{-5}$ | 10 | 0.8 | 0.37 | 0.27 | 0.38 |
| 2 | $1.5\times10-5$ | 22 | 0.4 | 0.25 | 0.09 | 0.38 |
| 3 | $1.2\times10^{-4}$ | 1.2 | 3.2 | 0.44 | 0.53 | 0.21 |
| 3 | $6\times10^{-5}$ | 2.5 | 1.6 | 0.30 | 0.24 | 0.21 |
| 3 | $3\times10^{-5}$ | 5.0 | 0.8 | 0.23 | 0.25 | 0.21 |
| 3 | $1.5\times10^{-5}$ | 10 | 0.5 | 0.20 | 0.10 | 0.21 |
| 4 | $1.2\times10^{-4}$ | 10 | 3.2 | 0.57 | 0.12 | 2.0 |
| 4 | $6\times10^{-5}$ | 20 | 1.6 | 0.65 | 0.28 | 2.0 |
| Average |  |  |  | 0.39 |  | 0.24 |

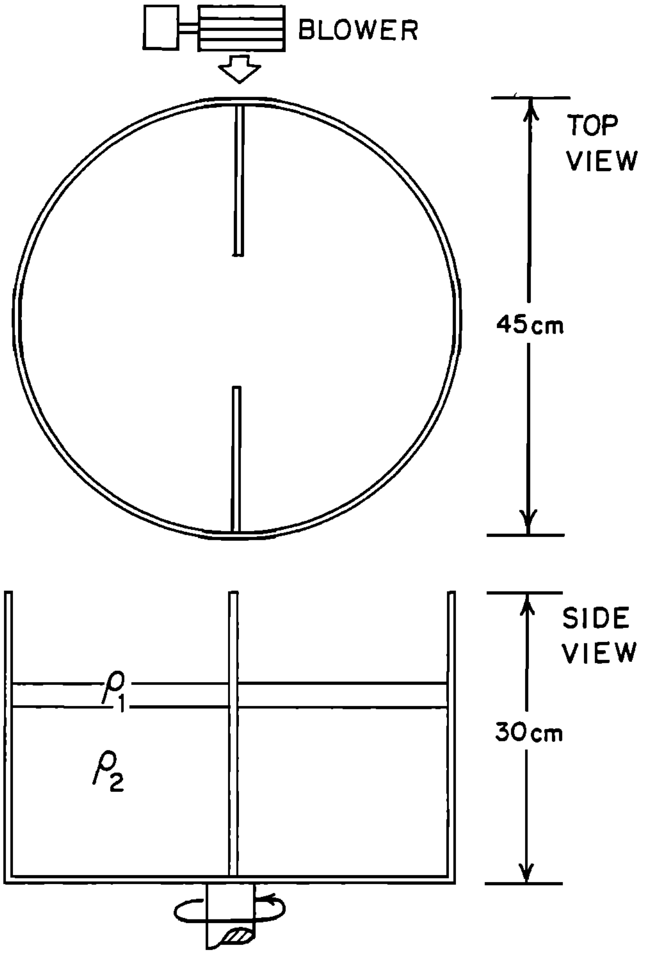

Fig. 14. Sketch of rotating tank used for wind-driven runs.

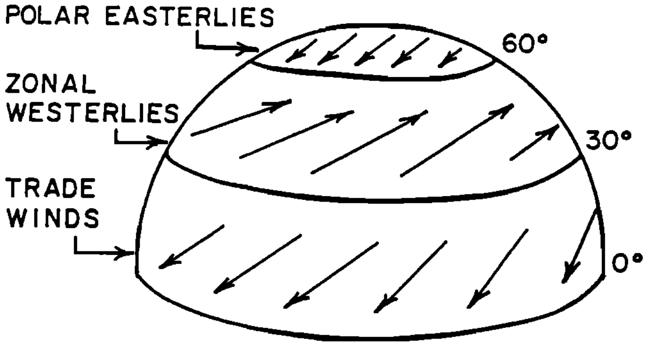

Fig. 15. Idealized surface wind circulation on a longitudinally uniform Earth.

cyclonic gyre began to develop (Figure 16). After a period of about 30 s almost all of the freshwater layer had been transferred to the "polar" basin, leaving only a thin layer around the periphery of the "subpolar" basin and exposing the deep layer at the surface in the central area (Figures 17 and 18). The fresh water is trapped in a circular lens in the "polar" basin which is shown clearly in side profile (Figure 19). The results are sketched in Figure 20. This polar gyre rotates rapidly in a clockwise direction with an angular velocity which is nearly the same as that of the tank but of opposite sign and thus remains nearly stationary relative to an external frame of reference. Rotation in the "subpolar" basin is cyclonic with an angular velocity nearly the same as that of the tank and remains nearly motionless relative to the tank frame of reference.

Several features of these experiments can be analyzed and explained by simple vorticity dynamics. Since the lower layer in the model was much deeper than the upper layer, a single-layer model was used in which gravity is reduced by the ratio of the density difference to the mean density. Depth of the Ekman layers was only about 1 mm, much less than upper layer depth, so the layer is taken to be inviscid with forcing by Ekman pumping on the top and dissipation through Ekman suction at the bottom. Friction on sidewalls will be ignored here, since their area was small relative to the area of the top and bottom surfaces. The Coriolis parameter is taken to be constant, since it can be demonstrated that in a rotating two-layer system, the depth of the upper layer in the basic state is constant and there is no vertical vortex stretching in the radial direction to simulate variation of the Coriolis parameter with latitude. The vertical vorticity equation derived from the inviscid shallow– water equations [*Gill*, 1982] is

$$\frac{d\omega}{dt} + (f+\omega)\left[\frac{\partial u}{\partial x} + \frac{\partial v}{\partial y}\right] = 0 \qquad (1)$$

where the Coriolis parameter is given by $f = 2\Omega$ in a tank with angular velocity $\Omega$, the relative vorticity is $\omega = \partial v/\partial x - \partial u/\partial y$, the total derivative is $d/dt = \partial/\partial t + u\,\partial/\partial x + v\,\partial/\partial y$, and the other symbols have their usual meanings.

Conservation of mass, which requires that changes in height of a water column be equated with the divergence of flow, which is composed of a horizontal flux through the sides of the column and a vertical flux through the top and bottom induced by Ekman pumping, is given by

$$\frac{d(h+\eta)}{dt} = -\frac{1}{\rho f}\,\mathrm{curl}\,\tau + \sqrt{\frac{\nu}{2f}}\,\omega \qquad (2)$$

where $h$ is the depth of the interface below the undisturbed water surface, $\eta$ is the elevation of the surface above the same reference level, $\nu$ is kinematic viscosity, and curl $\tau = [\partial\tau_y/\partial x - \partial\tau_x/\partial y]$ with $\tau_x$ and $\tau_y$ the components of surface wind stress. Elimination of horizontal divergence between (1) and (2) yields an equation for potential vorticity with forcing and damping terms,

$$\frac{d\omega}{dt} - \left[\frac{f+\omega}{h+\eta}\right]\left[\frac{d(h+\eta)}{dt} + \frac{1}{\rho f}\,\mathrm{curl}\,\tau - \sqrt{\frac{\nu}{2f}}\,\omega\right] = 0 \qquad (3)$$

Since the Rossby number is small in these experiments, a nearly geostrophic and hydrostatic balance is assumed. Hydrostatic balance requires the surface elevation $\eta = \delta h$, is a small number in these experiments allowing $\eta$ to be neglected in (3). The density defect is defined as $\delta = 2\,[\rho_1 - \rho_2/\rho_1 + \rho_2]$. The velocities for approximate geostrophic balance are

$$u = -\left[\frac{\delta g}{f}\right]\frac{\partial h}{\partial y}, \quad v = \left[\frac{\delta g}{f}\right]\frac{\partial h}{\partial x}$$

and relative vorticity is $\omega = \delta g/f\;[\partial^2 h/\partial x^2 + \partial^2 h/\partial y^2] = \delta g \nabla^2 h/f$.

This allows $\omega$ to be eliminated from (3), yielding a quasi-geostrophic vorticity equation with layer thickness $h$ as the dependent variable

TABLE 3. Typical Dimensional Parameters for Wind-Driven Experiments

| Parameter | Notation | Ocean | Laboratory |
|---|---|---|---|
| *Depth, upper layer* | $h_1$ | 100 m | 1.2 cm |
| *Depth, lower layer* | $h_2$ | 2000 m | 17.5 cm |
| Gap width | $L_1$ | $4.5\times10^5$ m | 10.2 cm |
| Basin width | $L_2$ | $10^7$ m | 43.8 cm |
| Density, upper | $\rho_1$ | 1026 kg $m^{-3}$ | 998 kg $m^{-3}$ |
| Density, lower | $\rho_2$ | 1028 kg $m^{-3}$ | 1025.3 kg $m^{-3}$ |
| Coriolis parameter | $f$ | $1.4\times10^{-4}$ $s^{-1}$ | 3.142 $s^{-1}$ |
| Acceleration due to Gravity | $g$ | 9.83 m $s^{-2}$ | 9.80 m $s^{-2}$ |
| Viscosity, vertical | $\nu_v$ | $10^{-2}$ $m^2$ $s^{-1}$ | $10^{-6}$ $m^2$ $s^{-1}$ |
| Viscosity, horizontal | $\nu_h$ | $10^{-4}$ $m^2$ $s^{-1}$ | $10^{-6}$ $m^2$ $s^{-1}$ |
| Current velocity | $U$ | 0.25 m $s^{-1}$ | $10^{-2}$ m $s^{-1}$ |
| Density defect | $\delta = 2[\rho_1 - \rho_2/\rho_1 + \rho_2]$ | $2\times10^{-3}$ | $25\times10^{-3}$ |
| Internal wave speed | $c = (\delta g h_1)^{1/2}$ | 1 m $s^{-1}$ | 0.054 m $s^{-1}$ |
| Internal radius of deformation | $R = c/f$ | 7.1 km | 1.7 cm |

TABLE 4. Dimensionless Parameters for Wind-Driven Experiments

| Parameter | Notation | Ocean | Laboratory |
|---|---|---|---|
| Rossby number | $R_0 = U/(fL_1)$ | $4\times10^{-3}$ | $3.1\times10^{-2}$ |
| Burger number | $S = R/L$ | $1.6\times10^{-2}$ | 0.17 |
| Hydrostatic number | $H_y = R/h_1$ | 71 | 1.4 |
| Ekman number | $E = \nu_v/(fh_2^2)$ | $1.8\times10^{-5}$ | $1.0\times10^{-5}$ |
| Depth ratio | $h_1/h_2$ | 0.05 | 0.068 |
| Length ratio | $L_1/L_2$ | $4.5\times10^{-2}$ | 0.23 |

$$\frac{\delta g}{f}\frac{\partial}{\partial t}\nabla^2 h - \frac{f}{h}\left[\frac{\partial h}{\partial t} + \frac{1}{\rho f}\operatorname{curl}\tau - \frac{\delta g}{f}\sqrt{\frac{\nu}{2f}}\,\nabla^2 h\right] = 0 \qquad (4)$$

Here the time-dependent terms have been linearized and we have assumed $\omega << f$ to be consistent with geostrophy. This quasi-geostrophic equation will be applicable only during early stages of spinup, since in the later stages of the tank runs it was observed that $\omega = f$ and that surface fronts appear. In order to evaluate the relative importance of the various terms in (4) the equation is scaled with the following characteristic values: $t' = t/T$, $(x', y') = (x, y)/L$, $h' = h/h_0$, $\tau' = \tau/\tau_0$. Scaled equation (4) is then

$$\left[\frac{R^2}{L^2}\right] \frac{1}{T} \frac{\partial}{\partial t'} \nabla'^2 h' - \frac{1}{h_0 h'} \left[ \frac{h_0}{T} \frac{\partial h'}{\partial t'} + \frac{\tau_0}{\rho f L} \operatorname{curl}' \tau' - \frac{R^2}{L^2}\right] \sqrt{\frac{\nu f}{2}}\, \nabla'^2 h' = 0 \qquad (5)$$

where $R = (\delta g h_0)^{1/2}/f$ is the Rossby radius of deformation. Since in these experiments $(R^2/L^2) = 0.028$, the first, or inertial, time term in (5) may be ignored. The third and fourth terms represent forcing and damping, respectively, and are retained in all cases as essential to the problem. With this approximation, (4), which is a dimensional equation, reduces to a linear equation for vorticity diffusion,

$$\frac{\partial h}{\partial t} + \frac{1}{\rho f} \operatorname{curl} \tau - \kappa \nabla^2 h = 0 \qquad (6)$$

where $\kappa = \delta g(\nu/2f^3)^{1/2}$ is the vorticity diffusivity. With this simplified equation it is possible to interpret a number of the features of wind-driven flow in the tank. In the early stages of development when velocities are still small, a near balance will exist between the first two terms of (6) as Ekman pumping forces water downward at the top to deepen the upper layer. At this early stage the growth rate of the layer,

$$\frac{\partial h}{\partial t} = -\frac{1}{\rho f} \operatorname{curl} \tau \qquad (7)$$

is the same as the vertical Ekman pumping velocity. In order to check the observed deepening of the layer against this simple relation, an estimate of wind stress curl is needed. Wind stress in this experiment may be calculated from the Ekman mass transport relation

$$M_y = \tau_x / f \qquad (8)$$

which gives the vertically-integrated transport normal to the wind stress vector. This transport will be established within one or two rotations of the tank after the wind commences. Since essentially all of the upper layer in one basin was transferred to the other basin in a period of about 60 s, the mass transport can be estimated from the known volume, gap width, and time. The value found by this method is $M_y = 0.64$ kg s$^{-1}$ m$^{-1}$. Then multiplication of this value by $f$ gives the maximum stress, $\tau_0 = 2.0$ Pa, at the gate region of the tank.

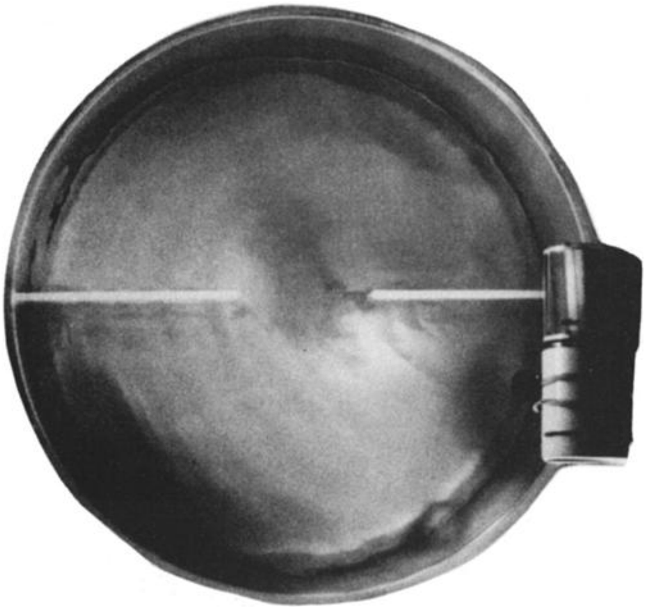

**Fig. 16.** Wind-driven experiment. Top view, one revolution (4 s) after blower was started.

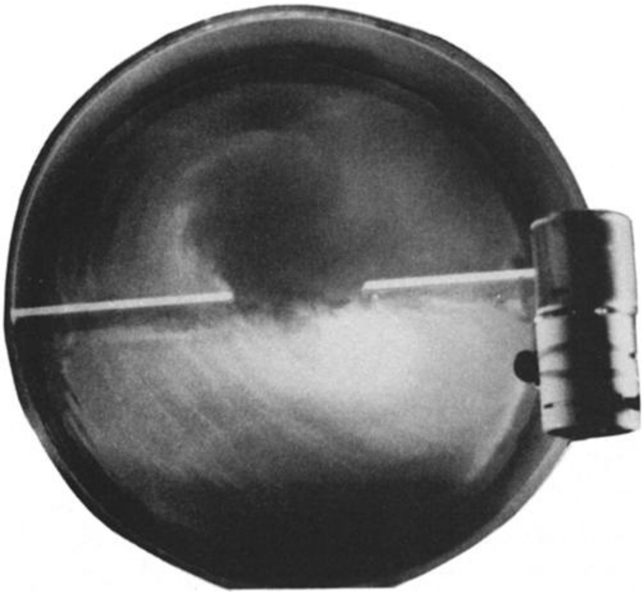

**Fig. 17.** Wind-driven experiment. Top view, three revolutions (12 s) after blower was started.

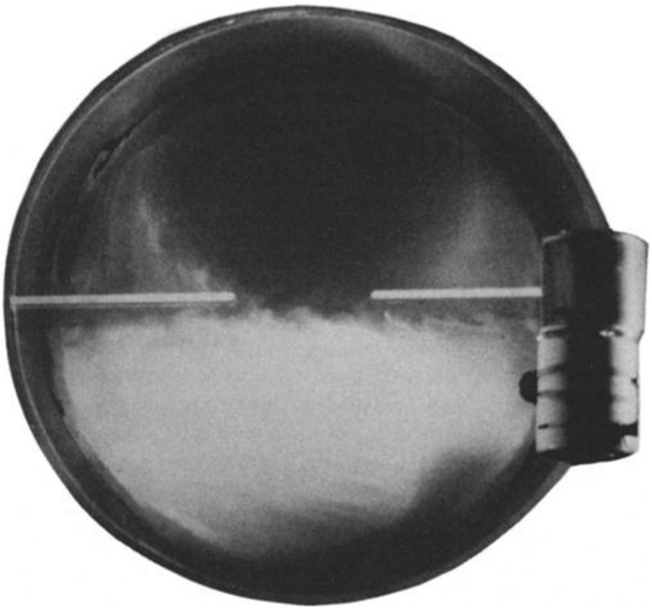

Fig. 18. Wind-driven experiment. Top view, eight revolutions (32 s) after blower was started. The dyed freshwater layer has been almost completely transfered to the "polar" basin where it is trapped in an anticyclonic gyre.

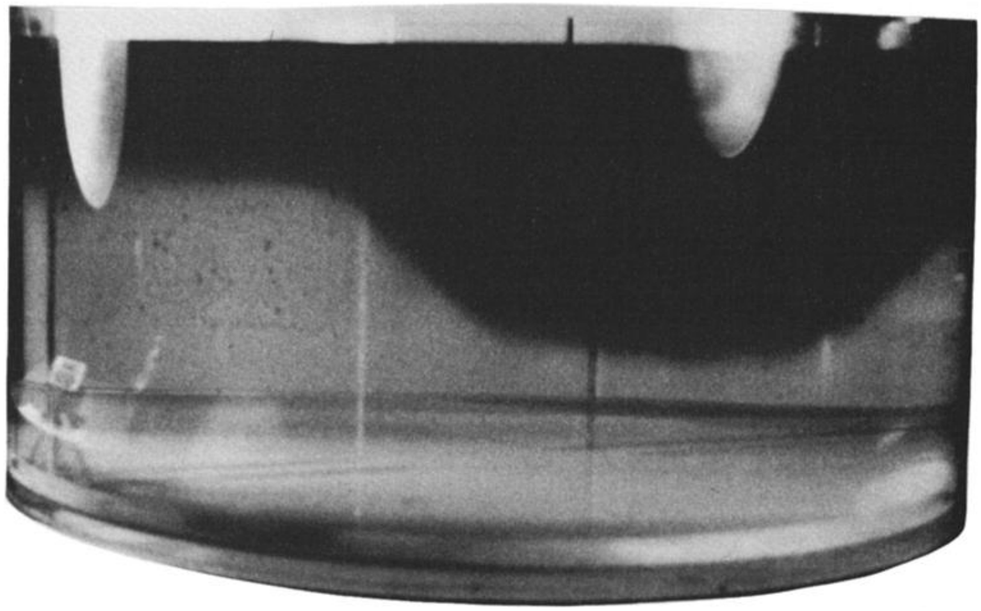

Fig. 19. Wind-driven experiment. Side view showing deep anticyclonic gyre of freshwater after 180 s.

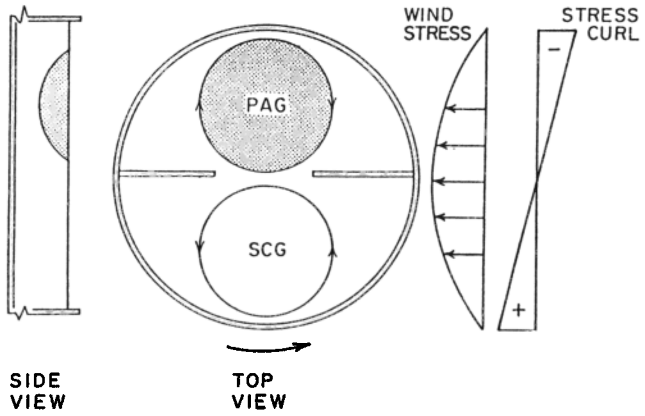

Fig. 20. Schematic diagram of results of wind-driven experiment after most of the freshwater layer has been transferred to the "polar" basin. Abbreviations are PAG for polar anticyclonic gyre and SCG for subpolar cyclonic gyre.

The curl of the wind stress may be estimated if the stress field is known. Details of the stress field were not measured, but a parabolic form of the profile is a reasonable assumption,

$$\tau_x = \tau_0 \left[\frac{y^2}{L^2} - 1\right] \qquad \tau_y = 0$$

The curl of the wind stress is then $-\partial\tau_x/\partial y = -2\tau_0\, y/L^2$, which varies from zero at $y = 0$ to a maximum value of $-2\tau_0/L$ at $x = 0, y = L$. To calculate the rate of deepening of the layer, take the mean value of the wind stress curl,

$$-\tau_0/L = 2.0 \text{ Pa}/0.45 \text{ m} = 4.4 \text{ Pa m}^{-1}$$

From (7) the rate of deepening for the upper layer is then calculated to be 1.4 mm s$^{-1}$, a value which agrees fairly well with the observation that the layer was 10 cm deep after about 60 s. After many revolutions a steady state will be reached which may be described by omitting the time term in (6),

$$\nabla^2 h - \frac{1}{\rho f \kappa} \operatorname{curl} \tau = 0 \qquad (9)$$

Solutions of this equation may be compared with qualitative observations, after many tank revolutions, of the thickness as shown in Figures 18 and 19. With the parabolic form of the wind stress, (9) becomes

$$\frac{\partial^2 h}{\partial x^2} + \frac{\partial^2 h}{\partial y^2} = -Fy \qquad (10)$$

where $F = 2\,\tau_0/\rho f \kappa L^2$. Boundary conditions are $h(x, y) = 0$ on the circle $x^2 + y^2 = L^2$.

The solution of (10) which satisfies the boundary conditions is

$$h(x, y) = -\frac{F}{8} y(x^2 + y^2 - L^2) \qquad (11)$$

Contours of surface height departures show an elevated dome in the upper semicircle and a depression in the lower semicircle corresponding with anticyclonic and cyclonic flow respectively (Figure 21). This quasi-geostrophic flow generally resembles the tank results, but limitations of the mathematical model do not allow it to describe the complete removal of the upper layer from the lower semicircle, since the linear model requires the upper layer to be present everywhere. Also the contours are not so perfectly circular in this calculation as they are in late stages of the actual experiment, and this also is likely due to the limitations of linearity.

A further test of the calculations against observation is the maximum thickness of the upper layer. Maximum thickness, as calculated from (11) using the wind stress arrived at earlier and the values in Table 3, occurs at $x = 0$, $y = L/3^{1/2}$ with a value, $h(0, L/3^{1/2}) = 0.88$ m. This calculated maximum depth is several times that of the layer observed in the center of the anticyclonic gyre after many minutes when an approximate steady state had been reached. The discrepancy indicates that linear Ekman theory is not adequate to predict the final steady state. This was anticipated earlier

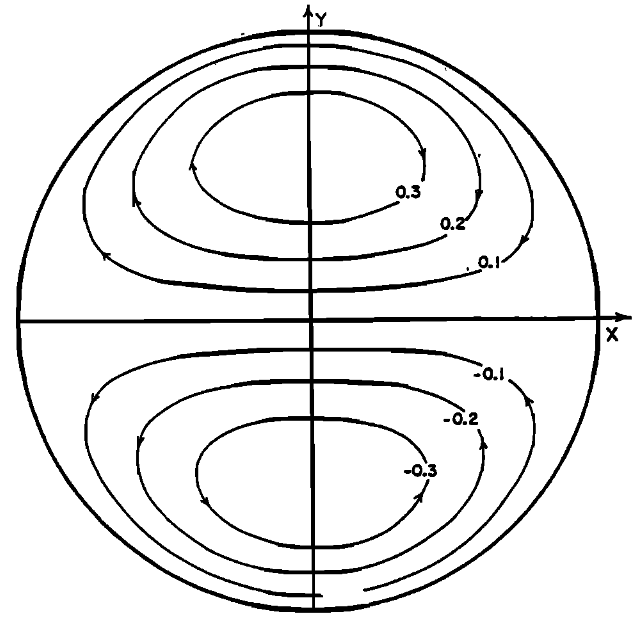

Fig. 21. Contours of surface height departure based on a linear vorticity model with a parabolic wind stress profile representing the polar easterlies. Contour heights are in dimensionless units, $[8/FL^3]\ h(x,y)]$. Arrowheads represent flow direction.

when the relative vorticity and the Coriolis parameter were found to have nearly the same magnitude after many revolutions. There must be more friction than than has been accounted for here. It may be that some eddy viscosity develops in these later stages to augment molecular viscosity. Sidewall friction has been ignored and may also represent some of the missing friction.

## LOCK-EXCHANGE THEORY

A theory for velocity of the flow and the shape of the interface is formulated here without the third underlying layer. Because of dynamical complexities involved with the two fluid layers lying over a third layer, it was felt that three layers was too complicated for a first attempt. In addition, it was anticipated that a quantitative laboratory experiment would be desirable to check the predictions, and a three-layer experiment did not appear to be practical. It is hoped that the formulation can be extended to the three-layer case in the future.

Consider two basins, basin 1 of depth $H_1$ with water of density $\rho_1$ and basin 2 of depth $H_2$ with water of density $\rho_2$. The two basins are separated by a straight smooth channel of depth $H_3$ with a closed gate. The surface of the water is initially the same everywhere, but upon removal of the gate the vertical interface between the two waters of different densities will experience a complicated collapse due to buoyancy forces. After some time we expect the light fluid to travel along the top of the channel out of basin 1 into basin 2 and the denser fluid to travel along the bottom of the channel out of basin 2 into basin 1. During the collapse, the sea surface between the two basins will have adjusted so that the volume flux of the two currents is equal.

The governing equations for the flow in the later stage are conservation of depth,

$$h_1(x) + h_2(x) = H_3 \tag{12}$$

conservation of potential vorticity

$$\frac{\partial v_1}{\partial x} + f = \frac{f h_1}{H_1} \tag{13}$$

$$\frac{\partial v_2}{\partial x} + f = \frac{f h_2}{H_2} \tag{14}$$

and thermal wind between the two layers

$$f(v_2 - v_1) = g' \frac{\partial h_2}{\partial x} \tag{15}$$

One can derive differential equations for $h_1$, $h_2$, $v_1$ and $v_2$ as follows: Take $\partial/\partial x$ of (15) and use (13) and (14) to get

$$\frac{\partial^2 h_2}{\partial x^2} - \frac{f^2}{g'}\left(\frac{1}{H_1} + \frac{1}{H_2}\right) h_2 = -\frac{f^2 H_3}{g' H_1} \tag{16}$$

We define $x$ as being zero in the middle of the channel. The solution of $h_2$ is

$$h_2 = \frac{H_3 H_2}{H_1 + H_2} + B \cosh \frac{x}{R} + A \sinh \frac{x}{R} \tag{17}$$

and from (12), the solution of $h_1$ is

$$h_1 = \frac{H_3 H_1}{H_1 + H_2} - B \cosh \frac{x}{R} - A \sinh \frac{x}{R} \tag{18}$$

where

$$R = \sqrt{\frac{g' H_1 H_2}{f^2 (H_1 + H_2)}}$$

To solve for velocity, use (13) and integrate:

$$v_1 = f \left\{ \frac{H_3 - H_1 - H_2}{H_1 + H_2} \right\} x - \frac{fRB}{H_1} \sinh \frac{x}{R} - \frac{fRA}{H_1} \cosh \frac{x}{R} + C \tag{19}$$

or use (14) and integrate

$$v_2 = f \frac{H_3 - H_1 - H_2}{H_1 + H_2} x + \frac{fRB}{H_2} \sinh \frac{x}{R} + \frac{fRA}{H_2} \cosh \frac{x}{R} + D \tag{20}$$

and (15) dictates that $C = D$.

Three constants remain to be determined, presumably by the inclusion of additional geometrical or dynamic considerations. Here, only the solution for the flat bottom ($H_1 = H_2 = H_3 = H$) will be investigated further, and then only with the assumption that the height profile is antisymmetric, so that $B = 0$. Under these conditions, equations (17)-(20) reduce to

$$h_1 = \frac{H}{2} - A \sinh \frac{x}{R} \tag{21}$$

$$h_2 = \frac{H}{2} + A \sinh \frac{x}{R} \tag{22}$$

$$v_1 = -\frac{fx}{2} - \frac{fRA}{H} \cosh \frac{x}{R} + C \tag{23}$$

$$v_2 = -\frac{fx}{2} + \frac{fRA}{H} \cosh \frac{x}{R} + C \tag{24}$$

Because of the symmetry of the profile, the assumption of equal and opposite volume flux through the lock region requires that $v_1 = -v_2$ at $x = 0$. This requires that $C = 0$, so only the constant $A$ remains to be determined.

*Gill* [1977] showed that the constant potential vorticity current has a Bernoulli function that is easily determined except for a constant. Since there is no dissipation in the current, this constant is conserved along streamlines. Therefore the symmetric solution for the current extends throughout the entire region from behind one nose through the passage to behind the other nose. The symmetric solution exists along the entire extent of the flow field.

Either energy considerations or Bernoulli's law has been used to solve for the final constant in hydraulics problems. Here we utilize the time-dependent energy equation by taking the dot product of the Euler equations with velocity for a two layer rotating fluid

$$\vec{u}\cdot\left\{\frac{\partial\vec{u}}{\partial t}+\vec{u}\cdot\nabla\ \vec{u}+f\ \vec{k}\ x\ \vec{u}-\nabla\ p+\rho\ g\ \vec{k}\right\}=0 \qquad (25)$$

and integrate over the entire volume including the region containing the transient noses of the currents as they move into the other basins. The volume integral of $u\cdot\nabla < \frac{1}{2}\ \vec{u}\cdot\vec{u} >$ $- < \vec{u}\cdot\nabla\ p >$ along with continuity $\nabla\cdot\vec{u}=0$ can be converted into a surface integral by Green's theorem for flux of kinetic energy into or out of the volume plus pressure work on the volume surface. We assume that the boundaries of the volume are sufficiently far from the noses that velocity is zero and therefore the surface integrals are zero. Hence we find a simple balance between change in potential energy and the increase in internal kinetic energy in the currents.

$$\frac{\rho}{2}\frac{\partial < \vec{u}\cdot\vec{u} >}{\partial t}+g\ < w\Delta\rho >= 0 \qquad (26)$$

This energy balance resembles that used by *Yih* [1980, p. 205].

We do not know the detailed flow in the nose region [*Stern*, 1980; *Stern, et al.*, 1982; *Griffiths and Hopfinger*, 1983] but we can assume that the nose is fully developed. Hence it will be self-similar between a time $t$ and a time $t+\delta t$. The similarity assumption requires that the volume of the moving nose region be unchanging, in which case we can set $c_i = Q_i/A_i$, where $Q_i$ is the volume flux of the *ith* current behind the nose and $A_i$ is the cross section area of the current (see Figure 22).

Thus the increase in internal kinetic energy in time equals $c_i$ times the area average of kinetic energy across the current. These are summed for the two on the left and the two on the right to give

$$\rho\ \frac{\partial}{\partial t}\frac{< v^2 >}{2}=\frac{\rho}{2}\ \left(\frac{Q_1}{A_1}+\frac{Q_2}{A_2}\right)$$

$$\left\{\int_{-\lambda/2}^{\lambda/2}\ v_2^2 h_2 dx+\int_{-\lambda/2}^{\lambda/2} v_1^2 h_2 dx\right\} \qquad (27)$$

Likewise, the increase in potential energy is equal to $c_i$ times the area of the current times the vertical displacement of the center of gravity of each column of width $dx$. The product of these is integrated across the currents and summed for the two noses to give

$$g < w\Delta\rho >= \frac{Q_2}{A_2}\int_{-\lambda/2}^{\lambda/2}\ g\Delta\rho\frac{h_2^2}{2}\ dx-$$

$$\frac{Q_1}{A_1}\int_{-\lambda/2}^{\lambda/2}\ g\Delta\rho\ h_1\left(\frac{h_1}{2}+h_2\right)\ dx \qquad (28)$$

Equations (27) and (28) are to be set equal, and since $Q_1 = Q_2$, $h_1 = H - h_2$, and $A_2 = A_2$, they simplify to

$$\int_{-\lambda/2}^{\lambda/2}\left[h_2\ v_2^2+h_1\ v_1^2-g'\left(\frac{H^2}{2}-h_2^2\right)\ dx\ \right]=0 \qquad (29)$$

Using equations (21)–(24) equation is (29) is found after some manipulation to reduce to

$$\frac{\lambda^3}{24\ R^3}+\frac{A^2}{H^2}\ \left[\frac{\lambda}{R}\ \left(1-\cosh\ \frac{\lambda}{R}\right)+4\ \sinh\right]\ \frac{\lambda}{R}\ =$$

$$\frac{\lambda}{R}\left(1+\frac{2A^2}{H^2}\right) \qquad (30)$$

where

$$\mathrm{A}\ \sinh\ \frac{\lambda}{2R}=\frac{H}{2} \qquad (31)$$

These two equations are satisfied for the values

$$\frac{\lambda}{2R}=2.5940 \qquad \frac{A}{H}=0.07514 \qquad (32)$$

Since $A$ was the last remaining unknown, volume flux can now be determined from the integral

$$Q_1=-Q_2=\int_{-\lambda/2}^{\lambda/2}\ h_1\ v_1\ dx \qquad (33)$$

$$Q_1=f\ A\ R\ \left(\frac{\lambda}{2}\ \cosh\ \frac{\lambda}{2R}\ -2\ R\sinh\ \frac{\lambda}{2R}\right) \qquad (34)$$

For the values of A and $\lambda$ given above, the formula reduces to

$$Q_1=0.156\ \frac{g'H^2}{f} \qquad (35)$$

The prediction of the width of the current and the volume flux has been the primary objective of the theory. Since it is quite believable to assume that the geostrophic assumption is valid, the qualitative form of the relation is not surprising so that the constant 0.156 is the central result of this exercise. Since predicting this value involved the use of a variety of assumptions, the volume flux prediction will be tested by laboratory experiment in the next section.

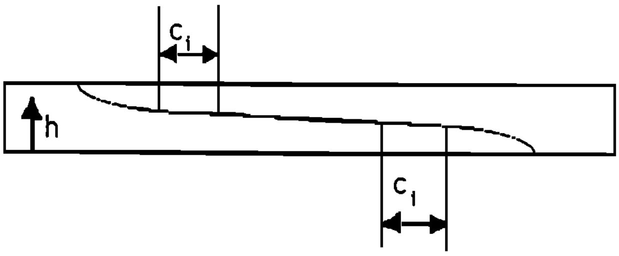

Fig. 22. Sketch of the change in energy and the extension of the nose region with velocity $c_i = Q_i/A_i$.

## LOCK-EXCHANGE EXPERIMENTS

Laboratory experiments were conducted to measure the transport by lock exchange flow with constant potential vorticity. The apparatus was a cylindrical tank 2 m in diameter with a 10-cm-high wall. The bottom was flat and level to better than 1 mm. Artificial walls were constructed as sketched in Figure 23 so that two basins were separated by a smooth 10 cm wide gap. Volume of each basin was measured by filling with water up to 5 cm deep and was 23500 cm$^{-3}$. The apparatus was placed on the 2 m rotating turntable at

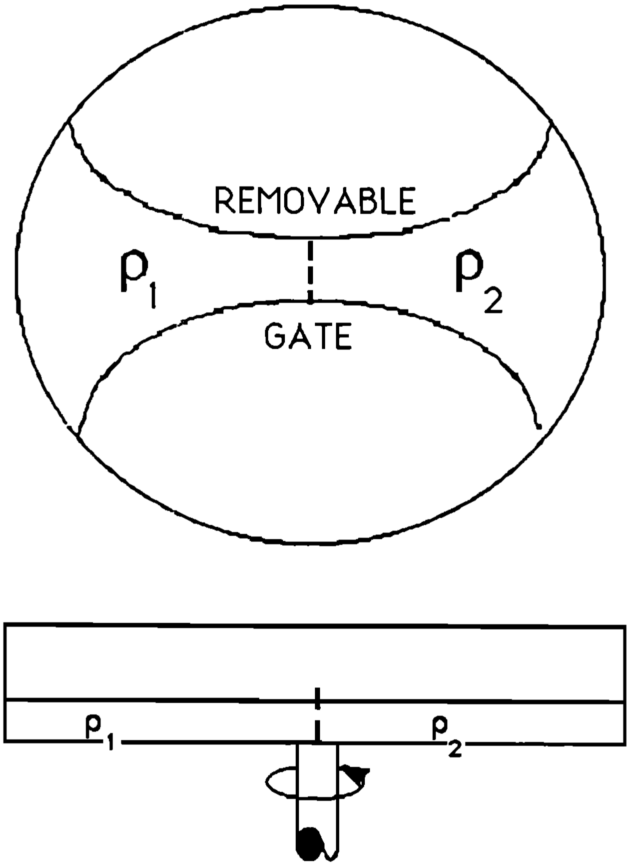

Fig. 23. Top view of the cylindrical basin used to test the constant potential vorticity theory.

the Coastal Research Center at Woods Hole Oceanographic Institution.

In a typical run, one basin was filled with fresh water and the other with slightly dyed water of known salinity. Samples of water were taken from each basin and the density measured. A removable watertight gate would separate the two basins. The turntable was then set into rotation and the period of rotation recorded. The depth of the water in the vicinity of the gate was also directly measured. After a motionless state was achieved in a rotating frame, the gate was removed and the density current would start. Within a few seconds the nose was seen to start into the other basin, curve to the right, and lead to a continuous flow into the other basin. When the nose was seen to have moved two thirds around the perimeter of the basin, the gate was replaced, the time of gate opening was noted, water in both basins was thoroughly mixed, and samples taken. The experiment could then be regarded as the initial conditions for a second experimental run with smaller initial density difference. The difference in dye intensity never got so small that it was impossible to see the nose, even though the color of the two waters gradually became similar.

In all, a total of 49 runs were conducted, 40 with a rotation period of approximately 15 s and 9 with a period of approximately a minute. Each run took between 20 and 40 min to conduct. The density of the samples was measured with a densiometer accurate to 0.0001 g cm$^{-3}$. The initial difference in density between the two basins $\rho_2 - \rho_1$ was calculated and multiplied by depth $H$. After each run the density change during the run $\Delta\rho$ was calculated by subtracting the density before the run from the density after the run for each basin and then averaging the absolute value of the change for the two basins. Density transport was then calculated from this result by dividing $\Delta\rho$ by the time $\tau$ the gate was left open.

The results are shown in Figure 24, where density transport was plotted as a function of density difference between the two basins times depth of the water. The data for 15 s were expected to be well within the rotating limit and were the most numerous observations. The data are compared with a line from a prediction of lock– exchange derived in section 4. The line was produced using the prediction of volume transport $Q_1 = 0.156\, g'h^2/f$ from lock-exchange constant potential vorticity theory equation (35). Volume flux is multiplied by $\rho_1 - \rho_2$ to predict a density flux. This density flux is divided by the volume of the basin to predict density change per unit time. Using the formula and the values for basin flux and rotation given above and a value of $g = 980$ cm s$^{-2}$, the prediction is that transport is proportional to 0.0077 $[(\rho_1 - \rho_2)H]^2$ as shown by the solid line. The data from experiments with a period of 15 s have an empirical best fit of 0.0039 $[(\rho_1 - \rho_2)H]^{1.88}$ as shown by the dashed line. This formula seems at first glance to not to agree very well with the rapidly rotating prediction. However, satisfactory agreement between data and theory is found to the left where $[(\rho_1 - \rho_2)H]$ is of the order $10^{-2}$ to $10^{-1}$. In that region some of the data lie above the theoretical curve but even more lie below. To the right, where $[(\rho_1 - \rho_2)H]$ gets closer to 1, the transport seems to curve over as though low rotation effects were beginning to be felt. Figure 24 has two additional features that give a clearer perspective of the observations. First the 60 s data are added as open squares. The data lie slightly above the fifteen second data. Second, a prediction for transport for nonrotating lock exchange transport was included as the top thick line. This was produced using a prediction for the velocity of nonrotating flow from *Yih* [1980] p. 207], $U = 0.71\ (gH(\rho_1 - \rho_2)/(\rho_1 + \rho_2))^{1/2}$. To use this formula to predict density flux, $U$ is multiplied

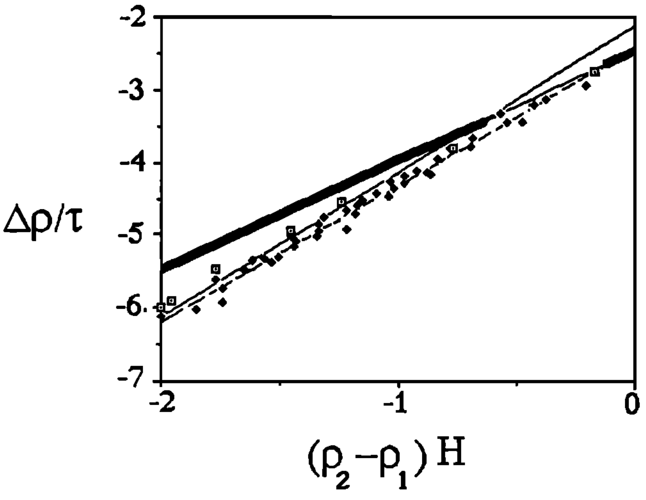

Fig. 24. Experimental measurements of density transport $\Delta\rho/\tau$ versus upstream parameter $I = (\rho_2 - \rho_1)H$. The data with a rotation period of approximately 15 seconds are given as diamonds. Data with a sixty-second period are open squares. The solid line is from a rotating lock exchange formula equation 35. Dashed line is a best fit line 0.0039 $((\rho_2 - \rho_1)H)^{1.88}$. The bold line is from nonrotating lock exchange theory.

by $HL/2$ to predict a volume flux which is again multiplied by $\rho_1 - \rho_2$ to predict a density flux. This density flux is divided by the volume of the basin to predict a density transport. The prediction is that transport is proportional to $0.0035[(\rho_2 - \rho_1)\ H]^{3/2}$. In comparing the data with both lines for rotating and nonrotating flow, one sees that the theory for nonrotating flow predicted far too large a transport to the left, where rotational effects were evidently important, but did come close to the data on the right. On the other hand, the rotating theory lies within the data on the left but lies above it on the right. The data with a rotation period of 60 s clearly lie above both the 15 s data and the rotating theory to the left, but below the nonrotating theory The empirical best fit for both the 60- and 15 s data is $0.0036[(\rho_1 - \rho_2)\ H]^{1.72}$. This has a power law almost exactly halfway between the rotating and nonrotating theory. To the right all the data lie slightly below both theories, but they appear to approach the nonrotating theory. Since the nonrotating theory is expected to be valid when it predicts less flow than the rotating theory, the data seem to confirm the nonrotating theory in this region.

## Lock-Exchange Calculation

A simple salt and volume balance for the Arctic Ocean–Norwegian Sea through Fram Strait will be made assuming that the Arctic Ocean is a "mediterranean basin" in a manner similar to that done by *Bye and Whitehead* [1975]. The model will incorporate conservation of volume

$$Q_i = Q_o + Q_f \tag{36}$$

where $Q_i$ is volume flux of water into the Arctic Ocean through Fram Strait, $Q_o$ is volume flux out of the Arctic Ocean through Fram Strait, and $Q_f$ is the volume of fresh water added to the Arctic Ocean through flows into it from other regions. The model will also incorporate conservation of salt in the simple form

$$S_i Q_i = S_o Q_o \tag{37}$$

By writing the conservation of salt in this way, one assumes that there is a simple correlation between the salinity of the currents into and out of the Arctic Ocean through Fram Strait. Although such a correlation is obeyed closely by the two-fluid laboratory models investigated here, the actual oceanic situation is more complicated. Equations (36) and (37) are now combined to give

$$Q_o \Delta S = S_i Q_f \tag{38}$$

We assume that $S_i$ and $Q_f$ are fixed by nature and that $Q_o$ and $\Delta S$ are unknown. The dynamic lock-exchange formula

$$Q_o = 0.156\ \frac{g' H^2}{f} = 0.156\ \frac{g\beta \Delta S H^2}{\rho f} = \frac{S_i Q_f}{\Delta S} \tag{39}$$

is then incorporated to reduce the system to one unknown. This gives the formula

$$\Delta S = \sqrt{\rho f S_i Q_f / 0.156 g \beta H^2} \tag{40}$$

To evaluate this, we take values of $\rho = 1027$ kg m$^{-3}$, $\beta = 0.71$ kg m$^{-3}$ $({}^\circ/_{\circ\circ})^{-1}$, $g = 9.8$ m s$^{-2}$ $S_i = 35\,{}^\circ/_{\circ\circ}$ as a representative number for oceanic salinity, and $f = 1.36 \times 10^{-4}$ s$^{-1}$. The value of $H$ to use would be that appropriate for the upper halocline water of the Arctic Ocean. Depending upon where one looked and what criterion one used, this could range from over 400 m to approximately 100 m in the center of the basin. The most sensible number appears to be $H = 200$ m that is representative of the 34.6 ${}^\circ/_{\circ\circ}$ haline depth near Fram Strait. The primary balance for fresh water in the Arctic Ocean is fresh water added by river runoff and freshwater removal by rafting of ice out of the ocean. We take $Q_f = 10^4$ m$^3$ s$^{-1}$ as the value of river runoff minus ice rafted south by currents from *Aagaard and Carmack* [1989]. These numbers in (40) give

$$\Delta S = 1.06\ {}^\circ/_{\circ\circ}$$

Aagaard and Carmack cite *Paquette et al.* [1985] as assigning the East Greenland Current an average salinity of 33.7. They also use for the Norwegian Sea a salinity of 34.6 and thus use values of inflowing and outflowing water differing by approximately $1\,{}^\circ/_{\circ\circ}$, a difference in agreement with this prediction. Thus it appears that the lock-exchange flow is consistent with the magnitude of freshwater renewal actually found in the Fram Strait region.

## Concluding Remarks

In this series of studies, assorted features in laboratory experiments that resemble the currents and transports in Fram Strait have been observed. In the first dam-break experiments, the transport of fluid from one basin to another by narrow boundary currents was clear. The width of the currents appeared to be scaled by the Rossby radius of deformation, although the photographs were not judged to be unambiguous enough to produce quantitative data. The current flowing from the fresh water side (which corresponds to the Arctic) to the intermediate side (which corresponds to the Greenland Sea) is a model of the East Greenland Current. The complexity of the real coastline and the bathymetry is lacking in the model. The laboratory current had a velocity that scales closely with the velocity scale $V_f/(g'h)^{1/2} = 0.4$. Using typical values of $g = 9.8$ m s$^{-2}$, $\Delta\rho/\rho = 1.8 \times 10^{-3}$ (from Figure 5), and $h = 200$ m, this gives an expected velocity of the East Greenland current of 0.77 m s$^{-1}$. This is roughly the velocity obtained by subtracting the wind-induced motion from observed ice motion [*Hunkins*, 1990].

The velocity of the current from the intermediate side to the freshwater side which corresponds to the West Spitsbergen Current was considerably slower and its velocity scale is not clear. The extension of the West Spitsbergen Current into the Arctic Ocean is poorly studied and its speed seems to be not documented, although observations of the tongue of highest temperature in the Arctic Ocean suggest that the current remains on the right-hand side of the Arctic Ocean for hundreds if not thousands of kilometers [*Hunkins*, 1990, Figure 7]. Therefore it is unclear whether the slowness of the laboratory current duplicates the ocean.

The extensive eddies in the laboratory experiments seem to duplicate the numerous eddies observed in the vicinity of Fram Strait. The eddies in the density-driven laboratory experiments roughly appeared to be a Rossby radius of deformation in size, and this appears true for the ocean eddies also. The eddies do not appear to be of only one sign (see especially Figures 8–11). The density-driven flows did not initiate a large cyclonic gyre south of the strait of much larger size, and one may suspect that the gyre in the Greenland Sea may arise from wind driving interacting with the density-driven flow. Combining buoyancy and wind driving is beyond the scope of the present investigation and must be left for further work.

If we assume the value of $A$ in section 4 is not fixed, as we have asserted there, the volume flux predicted by the lock-exchange theory reveals novel results when plotted as a function of $A$ as shown in Figure 25. For small $A$, the interface between the two fluids extends across the entire opening and there are local currents at the edge. There is a barotropic shear across the entire section (from equations (23) and (24)) that transports fluid in the "wrong" direction, i.e., low-density fluid toward the low-density end, and denser fluid toward the dense end. This barotropic transport is greater than the baroclinic transport within the side boundary layers. Conversely, the baroclinic component of the flow transports fluid in the "correct" direction i.e., low-density fluid away from the low-density end and dense fluid away from the dense end. The net result is density transport the "wrong" way for small $A$. For $A = H/2 \sinh(\lambda/2R)$, the boundary layers intersect the bottom and top and the current gets progressively narrower as $A$ increases above this value. The barotropic transport decreases and the total transport becomes more positive with increasing $A$. The predicted value of $A/H$ that satisfies the energy constraint lies above the point where the transport crosses zero. And finally as $A$ approaches infinity, the transport approaches 0.5. This reverse flow phenomenon has also been noted by *Pratt and Armi* [1990].

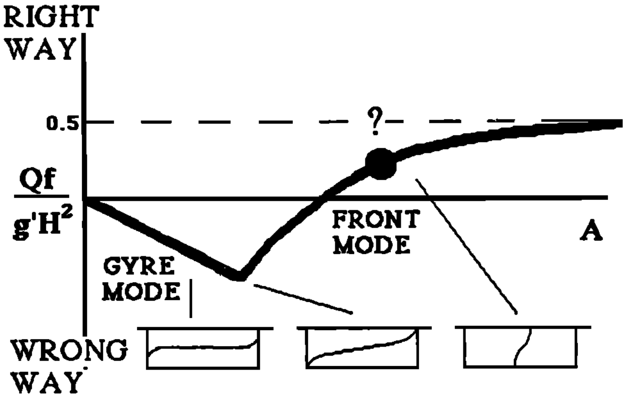

Fig. 25. Normalized density transport as a function of the last free parameter $A$. The sketched sections below the curve illustrate the position of the interface for the three values of $A$.

It is not clear whether the bizarre "wrong way transport" can ever arise in a physical situation although it had first been thought that the shear would correspond to gyre setup. However, this shear is anticyclonic, whereas the laboratory gyres had both signs of vorticity, and certainly the Greenland Gyre is cyclonic.

The wind-driven flow demonstrated that winds with a maximum easterly component to the north of Fram Strait would drive fresh water into the Arctic ocean. The laboratory results only pertain to an $f$ plane, of course. However, $\beta$ plane dynamics give the same result, since Sverdrup balance dictates that wind with cyclonic curl (easterlies north of the zero wind stress line) will produce northward drift. This drift could be expected to continue into the Arctic Ocean, since there is no observational basis for stopping northward flow at Fram Strait.

Given that there is abundent evidence that the Fram Strait flow is buoyancy driven [*Hunkins*, 1990], the apparent success of the lock-exchange formula is not really surprising, since it could be derived from a thermal wind relation alone. However, the use of that simple formula would require numerous assumptions. It is hoped that the lock-exchange derivation given and its being accompanied by quantitative laboratory data are more convincing.

Without doubt numerous real features have been omitted from this study. A list of these includes a shelflike bathymetric profile for the eastern wall, sidewall slope for all sides, the real coastal shape, continuous stratification, spherical geometry including the beta effect, sea ice, turbulence, and the actual temporal forcing (if it were known). Most of these, except for the challenging $\beta$ plane, could be incorporated in future studies, but it is hoped that this study provides the first approximation.

In closing, it must be remarked that the surface water of the Arctic Ocean is greatly undermixed. If the low-salinity water were mixed downward more vigorously, the exchange would be greater, and salinity difference between the surface water and deep water in the Arctic would be less. Equation (40) indicates that salinity difference would be inversely proportional to $H$, that was taken as the depth of the bottom of the halocline. But velocity would stay constant, since it is proportional to the square root of the product of density and $H$. Rafting of the Arctic ice, which removes more fresh water than the lock-exchange flow, is proportional to velocity of the East Greenland Current times the width of the current. The width is proportional to the Rossby radius of deformation, which is also proportional to velocity. So width also stays constant. Thus rafting is expected to be only weakly dependent on the mixing strength in the Arctic Ocean. It seems therefore that the processes that remove fresh water from the Arctic Ocean are independent of the vertical mixing coefficient there.

*Acknowledgments.* Support by the Office of Naval Research, Arctic Sciences, under contract N00014-87-K-0204 MH is acknowledged. The photographic work and valuable assistance with the laboratory experiments was provided by Robert E. Frazel, whom we thank. This work represents a collaboration between the two authors; however, section 3 was primarily an effort of the first author while sections 4 and 5 were primarily an effort of the second author, who was also supported by the Office of Naval Research, Coastal Science section, under grant N00014-89-J-1037 for studies of lock-exchange flows. Lamont-Doherty Geological Observatory contribution 4933; Woods Hole Oceanographic Institution contribution 7985.

## REFERENCES

Aagaard, K., Wind-driven transports in the Greenland and Norwegian seas, *Deep Sea Res., 17*, 281–291, 1970.

Aagaard, K., A synthesis of Arctic Ocean circulation, Rapp. P.-V. Reun. Cons. Int. Explor. Mer, 188, 11–22, 1989.

Aagaard, K., and E. C. Carmack, The role of sea ice and other fresh water in the Arctic circulation *J. Geophys Res., 94*, 14,485–14,498, 1989.

Aagaard, K., L. Coachman, and E. Carmack, Thermohaline circulation in the Arctic mediterranean seas, *J. Geophys. Res., 90*, 4833–4846, 1985.

Bourke, R., M. Tunnicliffe, J. Newton, R. Paquette, and T. Manley, Eddy near the Molloy Deep revisited, *J. Geophys. Res., 92*, 6773–6776, 1987.

Bye, J. A. T., and J. A. Whitehead, Jr., A theoretical model of the flow in the mouth of Spencer Gulf, South Australia, *Estuarine Coastal Mar. Sci., 3*, 477–481, 1975.

Carmack, E., Circulation and mixing in ice-covered waters, in *The*

*Geophysics of Sea Ice*, edited by N. Untersteiner, pp. 641–712, Plenum, New York, 1986.

Carmack, E., Large-scale physical oceanography of polar oceans, in *Polar Oceanography*, Part A, *Physical Science*, edited by W. O. Smith, Jr., pp. 171–222, Academic, San Diego, Calif., 1990.

Coachman, L., and K. Aagaard, Physical oceanography of Arctic and Subarctic seas, in *Marine Geology and Oceanography of the Arctic Seas*, edited by Y. Herman, pp. 1–72, Springer-Verlag, New York, 1974.

Colony, R., and I. Rigor, Arctic Ocean buoy program data report for 1 January 1990–31 December 1990, *Tech. Memo. APL-UW TM 10-91*, Appl. Phys. Lab., Univ. of Wash., Seattle, May 1991.

Colony, R., and A. Thorndike, An estimate of the mean field of ice motion, *J. Geophys. Res.*, *89*, 10,623–10,629, 1984.

Fleming, G. H., and A. J. Semtner, Jr., A numerical study of interannual ocean forcing on Arctic ice, *J. Geophys. Res.*, *96*, 4589–4603, 1991.

Foldvik, A., K. Aagaard and T. Torresen, On the velocity field of the East Greenland Current, *Deep Sea Res.*, *36*, 815–824, 1988.

Gill A. E., The hydraulics of rotating channel flow, *J. Fluid Mech.*, *80*, 614–670, 1977.

Gill, A., *Atmosphere-Ocean Dynamics*, 662pp., Academic, San Diego, Calif., 1982.

Ginsberg, A., and K. Fedorov, On the multitude of forms of coherent ice motions in marginal ice zones, in *Mesoscale/Synoptic Coherent Structures in Geophysical Turbulence*, edited by J. C. J. Nihoul and B. M. Smart, pp. 25–39, Elsevier, New York, 1989.

Griffiths, R. W., and E. J. Hopfinger, Gravity current moving along a lateral boundary in a rotating fluid, *J. Fluid Mech.*, *134*, 357–399, 1983.

GSP Group, Greenland Sea Project: A venture toward understanding of the oceans' role in climate, *Eos Trans. AGU*, *71*, 750–751, 754–755, 1990.

Hermann, A. J., P., B. Rhines, and E. R. Johnson, Nonlinear Rossby adjustment in a channel: Beyond Kelvin waves, *J. Fluid Mech.*, *205*, 469–502, 1989.

Hibler, W., III, and K. Bryan, A diagnostic ice-ocean model, *J. Phys. Oceanogr.*, *17*, 987–1015, 1987.

Hunkins, K., A review of the physical oceanography of Fram Strait, in *The Physical Oceanography of Sea Straits*, edited by L. Pratt, pp. 61–93, Kluwer, Academic, Boston, Mass., 1990.

Johannessen, J., O. Johannessen, E. Svendsen, R. Shuchman, T. Manley, W. Campbell, E. Josberger, S. Sandven, J. Gascard, T. Olaussen, K. Davidson, and J. Van Leer, Mesoscale eddies in the Fram Strait marginal ice zone during the 1983 and 1984 Marginal Ice Zone Experiments, *J. Geophys. Res.*, *92*, 6754–6772, 1987.

Jonsson, S., The structure and forcing of the large- and mesoscale circulation in the nordic seas, with special reference to the Fram Strait, doctoral dissertation, Univ. of Bergen, Bergen, Norway, 1989.

Jonsson, S., Seasonal and interannual variability of wind stress curl over the nordic seas, *J. Geophys. Res.*, *96*, 2649–2659, 1991.

Manley, T., K. Hunkins, and R. Muench, Current regimes across the East Greenland Polar Front at 78°40′ north latitude during summer 1984, *J. Geophys. Res.*, *92*, 6741–6753, 1987a.

Manley, T., J. Villanueva, J. Gascard, P. Jeannin, K. Hunkins, and J. Van Leer, Mesoscale oceanographic processes beneath the ice of Fram Strait, *Science*, *236*, 432–434, 1987b.

McDonald, B. E., and R. H. Dicke, Solar oblateness and fluid spin-down, *Science*, *158*, 1562–1564, 1967.

McLaren, A., M. Serreze, and R. Barry, Seasonal variations of sea ice motion in the Canada Basin and their implications, *Geophys. Res. Lett.*, *14*, 1123–1126, 1987.

Moritz, R., and R. Colony, Statistics of ice motion, Fram Strait to North Pole, in *Proc. of the Seventh International Conference on Offshore Mechanics and Arctic Engineering*, vol. IV, pp. 75–82, American Society of Mechanical Engineers, New York, 1988.

Paquette, R. G. , R. H. Bourke, J. F. Newton, and W. F. Perdue, The East Greenland Polar Front in autumn, *J. Geophys. Res.*, *90*, 4866–4882, 1985.

Piacsek, S., R. Allard, and A. Warn-Varnas, Studies of the Arctic ice cover and upper ocean with a coupled ice-ocean model, *J. Geophys. Res.*, *96*, 4631–4650, 1991.

Pratt, L. and L. Armi, Two-layer rotating hydraulics: Strangulation, remote and virtual controls, *Pure Appl. Geophys.*, *133*, 587–617, 1990.

Rudels, B., On the $\theta$-S structure in the northern seas, Implications for deep water circulation, *Polar Res.*, *4*, 133–159, 1986.

Rudels, B., On the mass balance of the Polar Ocean, with special emphasis on the Fram Strait, *Nor. Polarinst. Skr.*, *188*, 1–53, 1987.

Rudels, B., The formation of Polar Surface Water, the ice export and the exchanges through Fram Strait, *Prog. Oceanogr.*, *22*, 205–248, 1989.

Semtner, A., A numerical study of sea ice and ocean circulation in the Arctic, *J. Phys. Oceanogr.*, *17*, 1077–1099, 1987.

Serreze, M., A. McLaren, and R. Barry, Seasonal variations of sea ice motion in the Transpolar Drift Stream, *Geophys. Res. Lett.*, *16*, 811–814, 1989.

Stern, M. E., Geostrophic fronts, bores, breaking and blocking waves, *J. Fluid Mech.*, *99*, 687–704, 1980.

Stern, M. E., J. A. Whitehead, and B. L. Hua, The intrusion of a density current along a coast of a rotating fluid, *J. Fluid Mech.*, *123*, 237–265, 1982.

Stigebrandt, A., A model for the thickness and salinity of the upper layer of the Arctic Ocean and the relationship between ice thickness and some external parameters, *J. Phys. Oceanogr.*, *11*, 1407–1422, 1981.

Tchernia, P., *Descriptive Regional Oceanography*, 253 pp. Pergamon, New York, 1980.

Wadhams, P., and V. Squire, An ice-water vortex at the edge of the East Greenland Current, *J. Geophys. Res.*, *88*, 2770–2780, 1983.

Wadhams, P., A. Gill, and P. Linden, Transects by submarine of the East Greenland Front, *Deep Sea Res.*, *Part A*, *26*, 1311–1327, 1979.

Wood, R., and L. Mysak, A simple ice-ocean model for the Greenland Sea, *J. Phys. Oceanogr.*, *19*, 1865–1880, 1989.

Yih, C. S., Stratified Flows, 418 pp., Academic, San Diego, Calif., 1980.

---

K. Hunkins, Lamont-Doherty Geological Observatory of Columbia University, Palisades, NY 10964.

J. A. Whitehead, Department of Physical Oceanography, Woods Hole Oceanographic Institution, Woods Hole, MA 02543.

(Received October 25, 1991;
accepted January 3, 1992.)